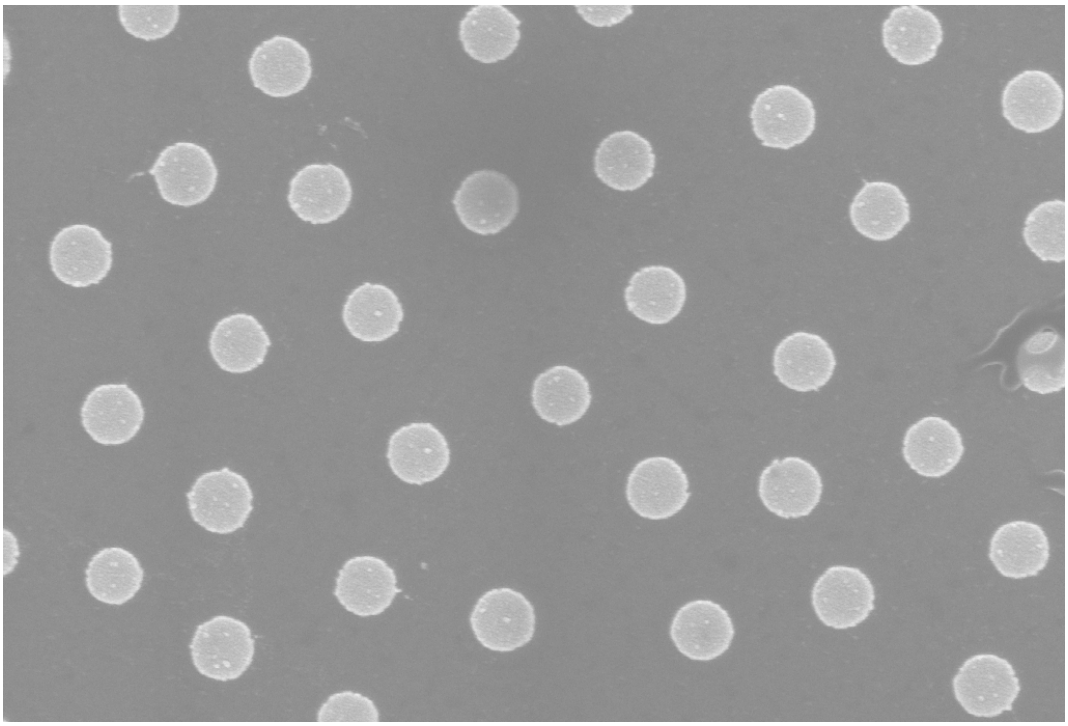

Pd-Pt nanoparticles for plasmonic sensing of hydrogen in humid environments

Master's thesis in Physics

William Colliander

DEPARTMENT OF PHYSICS

CHALMERS UNIVERSITY OF TECHNOLOGY
Gothenburg, Sweden 2025
www.chalmers.se

Master's thesis 2025

Pd-Pt nanoparticles for plasmonic sensing of hydrogen in humid environments

William Colliander

CHALMERS
UNIVERSITY OF TECHNOLOGY

Department Physics
Division of Chemical Physics
Chalmers University of Technology
Gothenburg, Sweden 2025

Pd-Pt nanoparticles for plasmonic sensing of hydrogen in humid environments
William Colliander

Supervisors: Christoph Langhammer, Carl Andersson, Sara Nilsson, Athanasios Theodoridis
Examiner: Christoph Langhammer, Department of Physics

Master's Thesis 2025
Department of Physics
Division of Chemical Physics
Chalmers University of Technology
SE-412 96 Gothenburg
Telephone +46 31 772 1000

Cover: $Pd_{85}Pt_{15}$ nanoparticles shown with scanning electron microscopy (SEM)

Typeset in LaTeX
Printed by Chalmers Reproservice
Gothenburg, Sweden 2025

Pd-Pt nanoparticles for plasmonic sensing of hydrogen in humid environments
William Colliander
Department of Physics
Chalmers University of Technology

Abstract

Using hydrogen as energy storage and as fuel in fuel cells are attractive ideas that have been investigated for decades. One of the big problems with using hydrogen for this purpose is that hydrogen, due to its small size, can easily escape from its containers, and only low concentrations are required for it to be explosive when mixed with oxygen. To help detect leaks and prevent accidents, a fast and reliable method for the detection of hydrogen gas is necessary. One of the most commonly used materials for this purpose is Pd, due to its ability to absorb H into interstitial sites in its lattice. The problem with Pd is that it is vulnerable to deactivation by several different compounds, one of which being water. This thesis aims to investigate a solution to this by incorporating Pt into the system. Several different compositions were fabricated ($Pd_{70}Pt_{30}$, $Pd_{85}Pt_{15}$, $Pd_{90}Pt_{10}$ and $Pd_{95}Pt_{5}$), and tested both as a bi-layered structure and alloyed together, in a humidity reactor. All systems show potential as hydrogen sensors in humid environments. However, how to clearly translate the complex signal output into readings of H_2 concentration remains unclear.

Keywords: hydrogen, sensing, nanoparticles, palladium, platinum

Acknowledgements

I would like to thank my supervisors, Carl Andersson, Athanasios Theodoridis and Sara Nilsson for their help and support with both fabrication and measurements as well as providing feedback and guidance on data analysis and writing. I would also like to thank my examiner Christoph Langhammer for his support and guidance.

William Colliander, Gothenburg, June 2025

List of Acronyms

Below is the list of acronyms that have been used throughout this thesis listed in alphabetical order:

CEM	Controlled evaporator mixer
Cr	Chromium
FWHM	Full-width half-maximum
H	Hydrogen
HCL	Hole-mask colloidal lithography
HOR	Hydrogen oxidation reaction
LFC	Liquid flow controller
LSPR	Localised surface plasmon resonance
MFC	Mass flow controller
NP	Nanoparticle
ORR	Oxygen reduction reaction
PDDA	Poly(diallyldimethylammonium chloride)
Pd	Palladium
PMMA	Poly(methyl methacrylate)
PS	Polystyrene
Pt	Platinum
PVD	Physical vapour deposition
SEM	Scanning electron microscopy

Contents

List of Acronyms **ix**

List of Figures **xiii**

1 Introduction **1**
1.1 Goals of this thesis 2

2 Theory **3**
2.1 Localised surface plasmon resonance (LSPR) and plasmonic sensing . 3
2.2 Metal-hydrogen interactions 4
2.2.1 H-Pd interactions 5
2.2.2 H-Pt interactions 5
2.3 Alloying 7

3 Methods **9**
3.1 Hole-mask colloidal lithography 9
3.2 Evaporation 10
3.3 Annealing 10
3.4 Scanning electron microscopy 11
3.5 Humidity-reactor 11

4 Results **13**

5 Conclusion & Outlook **21**

A Appendix 1 **I**

List of Figures

2.1 Schematic figure showing the localized surface plasmon resonance of a metallic nanoparticle. a) shows the response of the electrons of the NP when interacting with incoming light at the resonance condition ($\epsilon_1 = -2\epsilon_m$). b) The resonance appears as en extinction spectrum in the far field (Figure from ref [8]). 3

2.2 The typically used descriptors of peak position (λ_{peak}), extinction (Ext_{peak}) and full-width half-maximum ($FWHM$) of the LSPR extinction spectrum (Figure from ref [8]). 4

3.1 Schematic illustration of the steps followed during the hole-mask colloidal lithography (HCL) process: a) substrate cleaning, b) PMMA deposition via spin-coating, c) application of a positively charged PDDA coating, d) PS bead electrostatic self-assembly, e) Cr deposition via e-beam evaporation, f) tape-stripping to create exposed areas at the former positions of the PS beads, g) O2 plasma etch through the exposed areas to create holes. h) The final mask. Figure from ref [23]. 10

3.2 Schematic showing the unannealed and annealed NP. a) shows the unannealed sample is illustrated with Pd (blue) on the bottom and Pt (orange) on the top. b) shows the annealed NP where the Pd and Pt have formed a homogenous alloy. Both NPs have the dimensions of $d = 210\,\text{nm}$ and $h = 25\,\text{nm}$. 11

3.3 Schematic illustration of the humidity (X1) reactor setup. The humidified gas mixture and flow rate are controlled by a series of liquid flow controllers (LFCs) and mass flow controllers (MFCs) respectively, and are mixed in a controlled evaporator mixer (CEM), forming humidified gas. The sample is positioned inside a heated quartz tube with two optically transparent viewports allowing for transmission measurements. The humidity is measured using a humidity probe positioned close to the gas inlet. 12

4.1 SEM image of the annealed $Pd_{85}Pt_{15}$ NPs fabricated with HCL. Image at 32.76 thousand times magnification. 13

4.2 Overview of the whole measurement on $Pd_{95}Pt_5$ system after annealing. a) shows the hydrogen pulses (orange) with concentration varying between 0% to 4%, and the centroid peak (blue) of the plasmon extinction spectrum collected from the NPs. b) shows the total gas flow (orange), relative humidity (solid blue, between 0% and 80%) and the temperature of the sample (dashed blue, °C). 14

4.3 Example of how the response to a H_2 pulse looks up-close. The pulse starts at exactly 200 s after which a rapid blueshift of the peak is seen followed by a somewhat smaller redshift. Marked in the graph is the level before the pulse (upper line), the minimal point reached by the blueshift (red circle) and the level after the redshift happens (lower line). The descriptors shown in later figures are calculated from these values. $\Delta\lambda_{minpoint}$ is the difference between the lower level and the minimum point. $\Delta\lambda_{levels}$ is the difference between the two horizontal lines. 14

4.4 Comparison between the annealed and unannealed sample of $Pd_{95}Pt_5$ with 0% humidity. a) hydrogen pulses (orange) and the deviation in centroid peak from base level of the sample, both before annealing (blue) and after (red). b) $\Delta\lambda_{minpoint}$ for the before annealed (blue) and after (red) sample. c) $\Delta\lambda_{levels}$ for the before (blue) and after (red) annealed samples. 15

4.5 Comparison between the annealed and unannealed sample of $Pd_{95}Pt_5$ with 20% humidity. a) hydrogen pulses (orange) and the deviation in centroid peak from base level of the sample, both before annealing (blue) and after (red). b) $\Delta\lambda_{minpoint}$ for the before annealed (blue) and after (red) sample. c) $\Delta\lambda_{levels}$ for the before (blue) and after (red) annealed samples. 16

4.6 Comparison between the annealed and unannealed sample of $Pd_{95}Pt_5$ with 50% humidity. a) hydrogen pulses (orange) and the deviation in centroid peak from base level of the sample, both before annealing (blue) and after (red). b) $\Delta\lambda_{minpoint}$ for the before annealed (blue) and after (red) sample. c) $\Delta\lambda_{levels}$ for the before (blue) and after (red) annealed samples. 17

4.7 Comparison between the annealed and unannealed sample of $Pd_{95}Pt_5$ with 80% humidity. a) hydrogen pulses (orange) and the deviation in centroid peak from base level of the sample, both before annealing (blue) and after (red). b) $\Delta\lambda_{minpoint}$ for the before annealed (blue) and after (red) sample. c) $\Delta\lambda_{levels}$ for the before (blue) and after (red) annealed samples. 18

4.8 Summarising figure showing the descriptors $\Delta\lambda_{minpoint}$ and $\Delta\lambda_{levels}$ for all humidities for both the unannealed and annealed samples. a) and b) shows $\Delta\lambda_{minpoint}$ for all humidities for the unannealed and annealed samples respectively. Here it is clear that for 0% humidity there is no (or close to none) blueshift of the extinction peak. When humidity is present it is clear we get a blueshift that scales to the humidity present. c) and d) shows $\Delta\lambda_{levels}$ for all humidities for the unannealed and annealed samples respectively. Here it is also clear the system behaves very differently in dry conditions compared to in humid conditions. It is also clear that the behaviour in humid conditions scales with level of humidity. 19

A.1 Overview of the humidity measurments of the $Pd_{95}Pt_5$ sample before annealing. I
A.2 Overview of the humidity measurments of the $Pd_{70}Pt_{30}$ sample before annealing. II
A.3 Overview of the humidity measurments of the $Pd_{70}Pt_{30}$ sample after annealing. II
A.4 Overview of the humidity measurments of the $Pd_{85}Pt_{15}$ sample before annealing. III
A.5 Overview of the humidity measurments of the $Pd_{85}Pt_{15}$ sample after annealing. III
A.6 Overview of the humidity measurments of the $Pd_{90}Pt_{10}$ sample before annealing. IV
A.7 Overview of the humidity measurments of the $Pd_{90}Pt_{10}$ sample after annealing. IV
A.8 Comparison between the annealed and unannealed sample of $Pd_{70}Pt_{30}$ with 0% humidity. V
A.9 Comparison between the annealed and unannealed sample of $Pd_{70}Pt_{30}$ with 20% humidity. VI
A.10 Comparison between the annealed and unannealed sample of $Pd_{70}Pt_{30}$ with 50% humidity. VII
A.11 Comparison between the annealed and unannealed sample of $Pd_{70}Pt_{30}$ with 80% humidity. VIII

1

Introduction

Hydrogen is the lightest and the most abundant element in the universe. It is a highly reactive gas that also has high thermal conductivity and diffusivity. These properties have made it useful for several different applications. Hydrogen has a comparatively short history of being used by humans. It wasn't until the 1800s that we started using it for lighting, such as in the Döbereiner's lamp, and later for transport in airships and rockets, such as the infamous Hindenburg and NASA's spacecrafts during the 20th century. Today hydrogen is used for many different purposes, such as in the steel industry and as fuel in fuel cells. It also has several uses in catalytic processes, for example in the Haber-Bosch process for making ammonia [1].

To be able to turn away from using fossil fuels we need other media to store and release energy. Hydrogen gas shows promise in this regard due to it's high energy density and potential for carbon neutrality, since having water as the only product when utilized in a fuel cell. Using hydrogen as a means of storing and releasing energy attained from carbon neutral sources is not a new idea, as early as 1923 J. B. S. Haldane envisioned a future where wind power would generate electricity to create H_2 through electrolysis and in 1972 the term "hydrogen economy" was coined by John Bockris [2]. This refers to a sustainable chain of energy production, storage and usage facilitated by the use of hydrogen as the energy vector. It is based on the carbon neutral production of H_2 by electrolysis powered by sources like solar and wind power.

However, since hydrogen is very combustible when mixed with air and has a wide range of flammability between 4-75 vol %, safety systems are very important to utilize this technology safely[3]. Sensors are needed to both monitor the conversion efficiency in fuel cells and to detect any H_2 leaks along the supply chain. There have been several different types of H_2 sensors investigated during the last decades, but the type that this thesis focuses on are based on plasmonic nanoparticles.

Metallic nanoparticles (NPs), which this thesis focuses on, have been fabricated by humans for hundreds of years. One of the earliest examples of this is during the 4th century AD, when different types of artwork such as stained glass and cups were dyed by nanoparticles [4]. The Lycurgus cup is a famous example of this. But until the modern age their applications were limited to art. In the 19th century the first theoretical understanding of how the noble metal nanoparticles in these artworks gave them such beauty from their interaction with light was developed by Gustav Mie (1868-1957) [5]. Since then, the field has developed rapidly. Today, nanoparticles have a wide range of applications, from solar cells and catalysis to sensing and medicinal uses [6].

During normal operation the only exhaust product created in a hydrogen fuel cell is water, which means the humidity in the exhaust is very high. In addition to this, to monitor for leaks the sensor needs to be able to be placed in a technologically relevant environments, meaning it has to be able to deal with a wide range of atmospheric humidities. Pd is commonly used in sensing applications for H_2 due to its ability to readily dissociate and absorb H into its lattice. Unfortunately water deactivates Pd based hydrogen sensors by blocking sites for adsorption and dissociation of H_2 [7]. Developing a solution for Pd-based sensors in a humid environment is therefore needed.

Pt has the potential to solve the issue of deactivation by water due to its ability to, at ambient conditions, adsorb and dissociate H_2 and O_2 as well as catalyse the hydrogen oxidation reaction (HOR). The hope is to be able to combine the properties of Pd and Pt in one system to have a sensor that works well in a wide humidity range.

1.1 Goals of this thesis

The aim of this thesis is to investigate how these two materials, palladium and platinum, work in combination and how their different interactions with H_2 and humidity interplay. More specifically, in this thesis, nanoparticle based plasmonic hydrogen sensors constituted of Pd and Pt ($Pd_{70}Pt_{30}$, $Pd_{85}Pt_{15}$, $Pd_{90}Pt_{10}$ and $Pd_{95}Pt_5$), have been fabricated and their optical hydrogen sensing properties, both as layered, bimetallic systems as well as thermally annealed alloys, have been investigated in environments with different levels of humidity.

2

Theory

In this chapter the fundamentals of how plasmonic NPs can be used for sensing is introduced. As well as the relevant interactions between metals and gases present in a humid ambient environment.

2.1 Localised surface plasmon resonance (LSPR) and plasmonic sensing

Localised surface plasmon resonance (LSPR) are collective oscillations of the electron cloud of a metallic NP that can be excited by incoming electromagnetic waves (Figure 2.1 a)). This phenomena can be explained by the quasi-static approximation where the wavelength of the incoming light is assumed to be far grater than the size of the NP ($\lambda \gg d$). The incoming light that excites the plasmonic resonance is either absorbed or scattered, the combination of which is called extinction. For a sphere the cross section for the extinction can be expressed:

$$\sigma_{ext} = \frac{18\pi\epsilon_m^{3/2}V}{\lambda} \frac{\epsilon_2(\lambda)}{[\epsilon_1(\lambda) + 2\epsilon_m(\lambda)]^2 + \epsilon_2(\lambda)^2}, \tag{2.1}$$

$$\sigma_{ext} = \sigma_{abs} + \sigma_{sca}, \tag{2.2}$$

where λ is the wavelength of the light. Here V represents the volume of the NP, ϵ_1 and ϵ_2 represent the real and imaginary parts of the dielectric function of the material

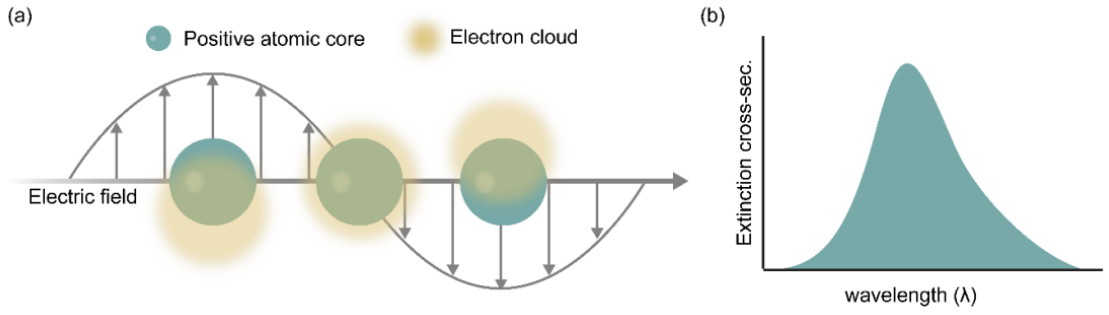

Figure 2.1: Schematic figure showing the localized surface plasmon resonance of a metallic nanoparticle. a) shows the response of the electrons of the NP when interacting with incoming light at the resonance condition ($\epsilon_1 = -2\epsilon_m$). b) The resonance appears as en extinction spectrum in the far field (Figure from ref [8]).

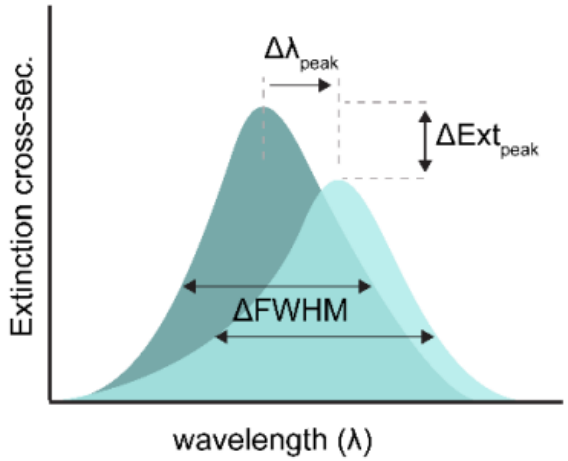

Figure 2.2: The typically used descriptors of peak position (λ_{peak}), extinction (Ext_{peak}) and full-width half-maximum ($FWHM$) of the LSPR extinction spectrum (Figure from ref [8]).

in the NP respectively, while ϵ_m is the dielectric function of the surrounding medium [8][9]. When the cross-section is maximised, which is achieved by minimising the denominator, i.e. when $\epsilon_1 = -2\epsilon_m$, a resonance condition occurs. This resonance condition gives rise to a peak in the extinction spectrum, however the peak is not singular and the width of the peak correlates with the plasmon damping in the NP, which is related to the the imaginary part of the dielectric function ϵ_2 (see Figure 2.1 b)).

From Equation 2.1 it is apparent that the extinction depends on both the dielectric function of the NP itself and its surroundings. This can be utilised for sensing applications. When the dielectric function of either the environment or the particle changes, from a reaction happening or structural changes in the NP, the way light interacts with it changes as well. This can then be seen as changes to the extinction peak. There are several ways to quantify these changes to the extinction, as seen in Figure 2.2. For this thesis, focus is placed on the change of the peak wavelength $\Delta\lambda_{peak}$ as the NPs are exposed to hydrogen (see section 2.2). However since the peak can be quite broad it can be difficult to track the exact peak of the spectrum. To make following how the signal changes more reliable to track small changes the centre of mass of the extinction peak was calculated and tracked instead, called the centroid peak. The centroid is calculated by fitting a high degree polynomial to the the spectrum data. The centroid differs somewhat from the maximum of the spectrum since the spectrum is not completely symmetrical around the peak. This method has been demonstrated to give the best signal to noise ratio for nanoplasmonic sensors [10].

2.2 Metal-hydrogen interactions

H_2 is highly attractive as a means of storing and releasing energy due to it's high gravimetric energy density 120 MJ/kg and potential for carbon neutrality. However

since H_2 is such a light gas it has a very low volumetric energy density of only 5.6 MJ/l, when at a pressure of 700 bar [11, 12], compared to approximately 34 MJ/l for gasoline and 36 MJ/l for diesel [13]. This can be increased slightly by storing it in liquid form, but this only increases the energy density to about 8 MJ/l [11]. This means that ways to store the hydrogen in other ways than in gas form is desirable. For this reason much attention has been placed on metals such as Ti, Pd and Ta since hydrogen easily forms a solid solution with these metals [14, 15, 16]. The formation of solid solutions between hydrogen and these metals varies widely depending on the conditions, with pressure and temperature being crucial factors.

2.2.1 H-Pd interactions

The reason why it is advantageous to use Pd specifically for H_2 sensors is due its ability to readily dissociate and absorb hydrogen into interstitial sites in its lattice. What sets Pd apart from other alternatives is its ability to do this at ambient conditions. H_2 first gets adsorbed to the surface of the Pd where it then dissociates and is able to diffuse into the Pd and occupy interstitial sites. This results in a solid solution at low pressures and a hydride, PdH_x at a temperature dependent critical pressure. The main difference between the solid solution of H in Pd and the hydride is that the hydride has a much more significant increase in its lattice parameter compared to the solid solution [17, 18, 19].

As mentioned in the previous section, both changes to the NP itself and to the immediate surrounding can be detected via changes to the extinction spectrum of the LSPR. The structural changes induced by the absorption of H_2 into the lattice of Pd NPs results in a change in the electronic density of states and thus changes the dielectric function, which can be detected as a shift towards longer wavelengths (redshift) of the extinction peak [20, 21]. The change in optical response of the NPs induced by the changes in the environment can be modelled by the Drude model as being proportional to the refractive index, $\lambda_{peak} \propto n_m$ [9]. Since H_2 has a lower refractive index than air (1.000132 for H_2 and 1.000293 for air [22]) this would lead to a shift towards shorter wavelengths (blueshift) of the plasmon peak. Since this is a very small change in refractive index the formation of solid solution or hydride will dominate the optical response. However, when in a humid environment there will be water adsorbed on the surface of the Pd NPs, blocking the H_2 from adsorbing and dissociating [7, 23, 24, 25]. One way to solve this problem that has been investigated is by operating at a higher temperature making water more easily desorb from the surface [20]. However, it is not a perfect solution since the energy requirements increase with increased operating temperature. Furthermore, too high temperatures may eliminate the response of the system entirely due to H_2 dissolving into the Pd no longer being thermodynamically favourable.

2.2.2 H-Pt interactions

Pt is not as good as Pd at absorbing H into its lattice and forming a hydride, since it requires much higher temperatures and pressures to achieve this [26]. However, Pt has very good catalytic properties for various reactions, of which most important

for this thesis is the oxygen reduction reaction (ORR) and the hydrogen oxidation reaction (HOR) [27, 28, 29]. Additionally both adsorption and dissociation of H_2 and O_2 occur at ambient conditions on Pt.

In sensing applications Pt has many different uses. For example in resistance based sensing applications it can be used both in combination with other sensing materials, as a catalyst for dissociation of H_2, or as the sensing material itself [23, 30]. The highly efficient and exothermic HOR can be utilised for thermocatalytic sensing of H in an O rich environment (i.e. air) since the reactions cause a temperature increase which can both be directly measured, and measured through change in resistance [24, 31].

As stated above, Pt is a well known catalyst of the HOR. In this reaction, adsorbed H, O and OH react to form H_2O. The reaction takes place via the Langmuir-Hinshelwood mechanism where the reactants adsorb, dissociate and thermally diffuse along the surface to react [32]. The reaction can happen in a few different ways [23, 32],

$$O_{ads} + H_{ads} \longrightarrow OH_{ads} \tag{2.3}$$

$$OH_{ads} + H_{ads} \longrightarrow H_2O_{des} \tag{2.4}$$

$$OH_{ads} + OH_{ads} \longrightarrow H_2O_{des} + O_{ads}. \tag{2.5}$$

The subscripts "ads" and "des" refers here to the species being adsorbed to the surface and being desorbed in gas phase respectively.

In dry conditions with an O_2-rich environment (such as in air) the Pt surface will be covered by dissociated O. Since O has high electronegativity it will draw out electrons from the surface of the Pt, which decreases the electron density at the surface, increasing the real part of the dielectric function of the NP. This results in a redshift of the plasmon peak. When then H_2 is introduced, Pt catalyses the HOR forming H_2O that desorbs from the surface. This means that the O layer on the surface is removed, causing a blueshift. Furthermore, some sites previously occupied by O can now be occupied by dissociated H, which being much less electronegative, donates electrons to the Pt causing further blueshift of the plasmon peak.

When there is humidity present there will be some amount of water and OH groups adsorbed on the surface of the Pt, in addition the O from the air. Due to the higher refractive index of water compared to air (1.333 for water and 1.000293 for air [22]) this covering will induce a redshift of the plasmon resonance peak. This is derived from the Drude model that, as mentioned previously, states that $\lambda_{peak} \propto n_m$. When then H_2 is introduced into the background gas, the catalysed HOR will remove OH groups, as seen in Equation 2.4. The exothermic nature of the HOR will also make adsorbed water more easily thermally desorb from the surface, thereby reducing the refractive index of the surroundings and causing a blueshift of the plasmon resonance peak. Similar to the dry conditions, some dissociated H will take the place of H_2O and OH, donating electrons to the surface and inducing further blueshift of the extinction peak. As such there are two effects, the change in refractive index of the surrounding medium and the change in electron density at the surface of the NP, that contribute to a optical blueshift in the plasmon extinction peak.

2.3 Alloying

Combining materials, especially metals, to enhance or modify their properties has been a staple of human society since the bronze age. Taking two or more materials and combining them to form something greater than the sum of its parts. As the example with bronze, both tin and copper are relatively soft. But when alloyed together they become strong enough to make tools and weapons with. There are several ways to form an alloy between two or more metals, including melt mixing and powder metallurgy. However, the one of interest for this thesis is solid-state diffusion. To form an alloy via solid-state diffusion the metal components are placed in contact with each other and annealed at high temperatures to allow for atomic diffusion between them, if that is thermodynamically possible [33, 34]. It is however a very slow process. At most, solid-state diffusion moves on the order of μm/s at the ideal conditions (close to the melting point of the metals) [23, 35]. This means that time and temperature are key factors for the alloy formation via solid-state diffusion. Other factors like material properties, melting point and diffusion coefficient also impacts the alloying process. In general, as well as in this thesis, the annealing is done far below the melting temperature of the metals. This works well for applications on NPs since the small size lowers the distance the atoms need to diffuse for alloy formation.

In this thesis the interaction between Pd and Pt and how the interplay between their response to H_2 pulses in both dry and humid conditions is investigated. To further understand how their different properties interact both alloyed NPs and a unannealed layered structure are tested.

3
Methods

In this chapter, methods for the fabrication of the nanoparticles and methods of measuring their performance as sensors will be described. All of the nanofabrication in this thesis was carried out at Chalmers' cleanroom facilities (MyFab).

3.1 Hole-mask colloidal lithography

To fabricate the NPs studied in this thesis, the process of hole-mask colloidal lithography (HCL) was utilised. HCL is a versatile bottom-up nanofabrication method that relies on colloidal self-assembly. This can be achieved by having a positively charged substrate and negatively charged colloidal particles, resulting in the particles being repelled by each other but attracted to the surface, forming a uniform layer on the substrate [36]. One big advantage of HCL is the ability to produce a large number of masks at the same time.

The substrates that were going to be used needed to be cleaned before any deposition could be done. The substrates used were of both fused silica and silicon (Si) wafers ($10 \times 10 \times 0.5\,\mathrm{mm}^3$). The fused silica was used as substrate for all optical measurements that were performed in the humidity reactor (see section 3.5). The Si substrate was used for the scanning electron microscopy (SEM) imaging of the NPs since it has higher conductivity and hence avoid any charging effects that could occur on an insulating material (such as fused silica) when used in SEM. To clean the substrates they were washed in both acetone and isopropanol in a ultrasonicator for 5 minutes each (Figure 3.1 a)).

The first step after the substrates were cleaned was depositing a layer of Poly(methyl methacrylate) (PMMA) by spin-coating (Figure 3.1 b)). The wafer was placed on a spin chuck and a few drops of the PMMA solution applied. It was then spun at 2000 rpm for 60 s to achieve a thickness of roughly 260 nm. After the PMMA solution was evenly coated on the wafer surface, it was baked at 170 °C for 3 minutes to remove the remaining solvent. To induce hydrophobicity in the PMMA surface, it was treated with an O_2 plasma for 5 s.

On top of the layer of PMMA, a layer poly(diallyldimethylammonium chloride) (PDDA) is then drop-coated on (Figure 3.1 c)). After an incubation time of 1 minute the sample was washed with Milli-Q water and dried with N_2 gas. In the next step Polystyrene (PS) beads with a diameter of 210 nm are deposited on the PDDA (Figure 3.1 d)). This was again done by drop-coating the sample with a solution of PS.

On top of the PDDA and the PS beads, chromium (Cr) was deposited via

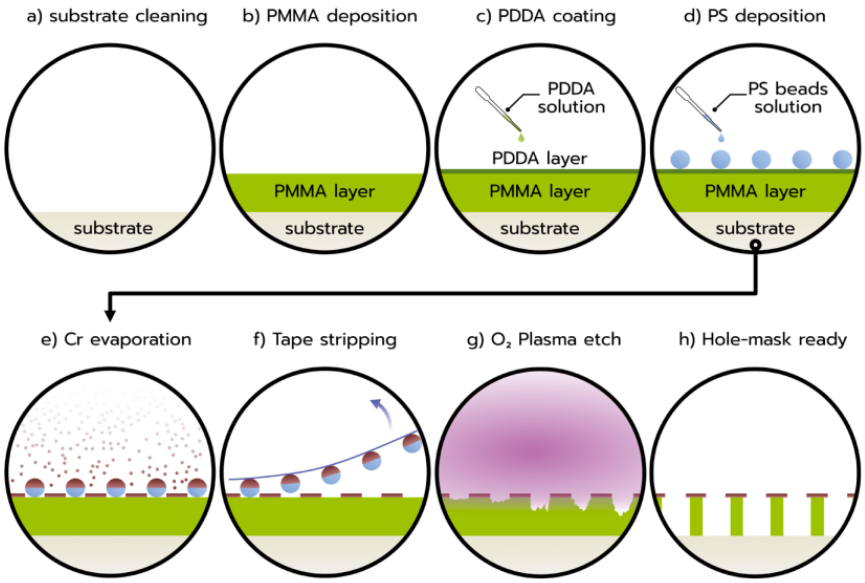

Figure 3.1: Schematic illustration of the steps followed during the hole-mask colloidal lithography (HCL) process: a) substrate cleaning, b) PMMA deposition via spin-coating, c) application of a positively charged PDDA coating, d) PS bead electrostatic self-assembly, e) Cr deposition via e-beam evaporation, f) tape-stripping to create exposed areas at the former positions of the PS beads, g) O2 plasma etch through the exposed areas to create holes. h) The final mask. Figure from ref [23].

e-beam evaporation (Figure 3.1 e)). Tape is then used to remove the Cr covered PS beads, leaving holes in the Cr cover (Figure 3.1 f)). The PMMA and PDDA under the holes in the Cr cover were then etched away using an O_2 plasma for 5 min (Figure 3.1 g)). This then results in a finished mask ready for deposition (Figure 3.1 h)).

3.2 Evaporation

When the masks have been created using HCL, they are ready for the deposition of the metals that will make up the NPs. This is done using e-beam physical vapour deposition (PVD). To calculate how thick the layers of Pd and Pt should be to obtain the desired composition, it was assumed that the resulting NP will have the shape of a truncated cone with 60 ° angle. Using that assumption together with the atomic density of the materials and the specified size of the NPs ($d = 210\,\text{nm}, h = 25\,\text{nm}$).

3.3 Annealing

The NPs produced by the HCL process have a layered structure from the evaporation. To transform the layered structure of the particles into homogeneous alloy of Pd and Pt, they were annealed at 500 °C in 4 % H_2 in Ar for 24 h. In Figure 3.2 a schematic of how the annealing affects the NPs is shown.

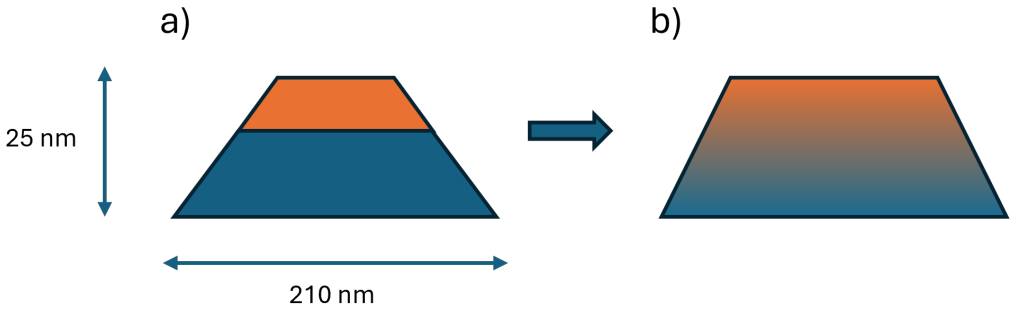

Figure 3.2: Schematic showing the unannealed and annealed NP. a) shows the unannealed sample is illustrated with Pd (blue) on the bottom and Pt (orange) on the top. b) shows the annealed NP where the Pd and Pt have formed a homogenous alloy. Both NPs have the dimensions of $d = 210\,\text{nm}$ and $h = 25\,\text{nm}$.

3.4 Scanning electron microscopy

To get an overview of how the particles look and to verify that the fabrication process was successful, the samples were examined by scanning electron microscopy (SEM). As stated above, the fabrication on NPs for the SEM imaging was carried out on silicon (Si) wafers, instead of the fused silica that was used for the samples measured on in the humidity reactor. This is due to the higher conductivity of the Si removes charging effects that can occur when using insulating materials in SEM.

3.5 Humidity-reactor

The main experiments were carried out in the humidified flow (X1) reactor (Insplorion AB) (for schematic see Figure 3.5). In this reactor, it is possible to control both gas-flow, temperature and humidity. The setup consists of mass flow controllers (MFCs, Bronkhorst High-Tech B.V.) that control the gas flow into the main chamber which is a quartz tube (volume of $\sim 190\,\text{mL}$). Incorporated into the flow line is also a liquid flow controller (LFC, Bronkhorst High-Tech B.V.) that controls the flow of H_2O. Before reaching the main chamber, the gases and the water are mixed in a controlled evaporator mixer (CEM, Bronkhorst High-Tech B.V.) where the H_2O is evaporated, forming humidified gas. The tube has optical access for transmittance measurements. At the chamber inlet there is a humidity and temperature probe (HMP7, Vaisala) that monitors the humidity of the incoming gas. The temperature of the reactor was measured by a K-type thermocouple placed on the back of one of the samples measured. This temperature readout was then used as input signal for the closed-loop temperature control system (Eurotherm 3216) in a feedback manner. The samples are illuminated by an unpolarized halogen white-light source (AvaLight-HAL, Avantes) connected via a bifurcated optical fibre (FCB-UV600-2, Avantes BV) equipped with collimated lenses. The transmitted light is then collected and sent to a dual channel fibre-coupled fixed-grating spectrometer (AvaSpec-ULS2048CL-2-EVO, Avantes BV).

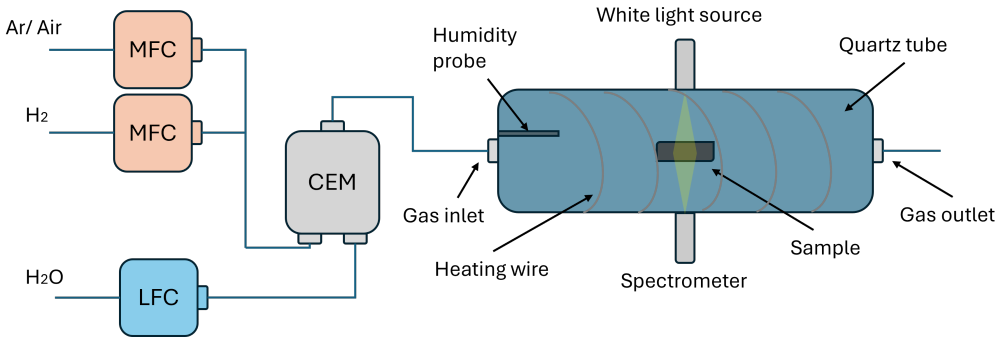

Figure 3.3: Schematic illustration of the humidity (X1) reactor setup. The humidified gas mixture and flow rate are controlled by a series of liquid flow controllers (LFCs) and mass flow controllers (MFCs) respectively, and are mixed in a controlled evaporator mixer (CEM), forming humidified gas. The sample is positioned inside a heated quartz tube with two optically transparent viewports allowing for transmission measurements. The humidity is measured using a humidity probe positioned close to the gas inlet.

4

Results

In this chapter the results of the SEM imaging and the optical hydrogen absorption measurements in increasing humidity backgrounds are presented. For the sake of brevity, only the hydrogen absorption measurements of system $Pd_{95}Pt_5$ will be discussed here (for the full data set of both absorption and desorption on all systems $Pd_{70}Pt_{30}$, $Pd_{85}Pt_{15}$, $Pd_{90}Pt_{10}$ and $Pd_{95}Pt_5$, see Appendix A). It can be noted though that the other systems follow similar trends to that of $Pd_{95}Pt_5$.

In Figure 4.1 a SEM image of the $Pd_{85}Pt_{15}$ is shown. The SEM investigation was done to confirm that the fabrication process was successful. Since the NPs visible in the figure are of the right shape and size (disks with a diameter of 210 nm), we can confirm that the fabrication process was successful.

In Figure 4.2 an overview of the entire measurement series can be seen. Each hydrogen pulse extends for 300 s followed by a 600 s wait time to let the system equilibrate. One thing to note is that in all figures showing the measurement at 20 % humidity the first, lowest concentration pulse (0.063 % H_2) is missing. This is simply due to an error in the protocol used for the measurements. However as the aim of this thesis is to mostly study general trends of the optical response of the nanoparticles at different humidity levels and hydrogen concentrations, the missing pulses has little impact on the results. To quantify the different responses from the different processes two descriptors were defined $\Delta\lambda_{minpoint}$ and $\Delta\lambda_{levels}$ (see Figure 4.3 for details).

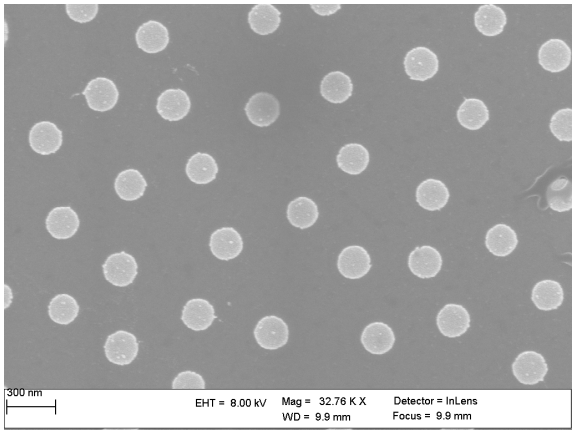

Figure 4.1: SEM image of the annealed $Pd_{85}Pt_{15}$ NPs fabricated with HCL. Image at 32.76 thousand times magnification.

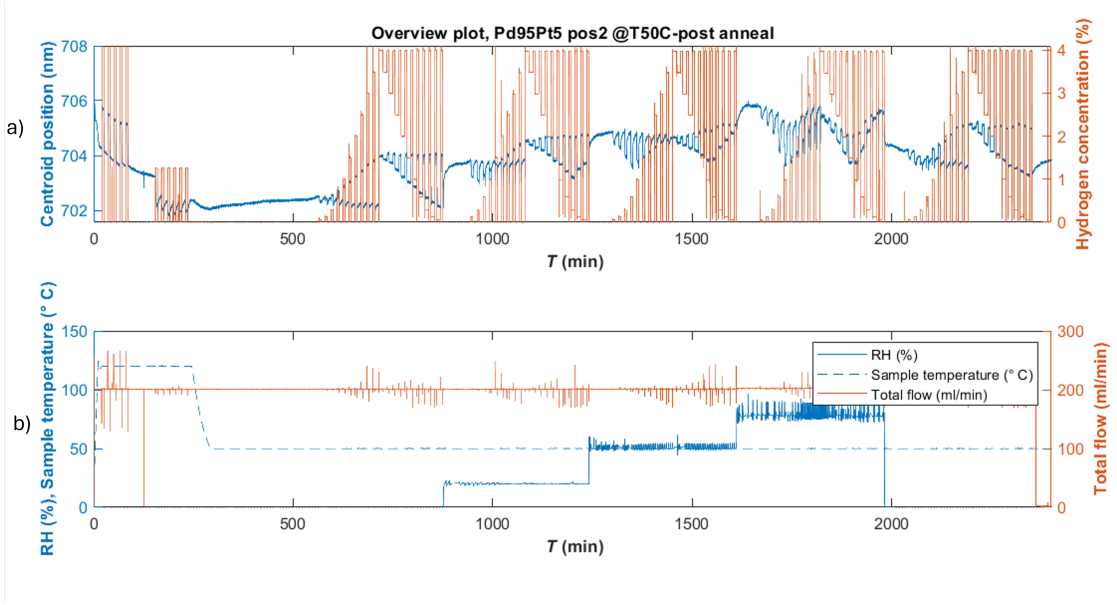

Figure 4.2: Overview of the whole measurement on $Pd_{95}Pt_5$ system after annealing. a) shows the hydrogen pulses (orange) with concentration varying between 0% to 4%, and the centroid peak (blue) of the plasmon extinction spectrum collected from the NPs. b) shows the total gas flow (orange), relative humidity (solid blue, between 0% and 80%) and the temperature of the sample (dashed blue, °C).

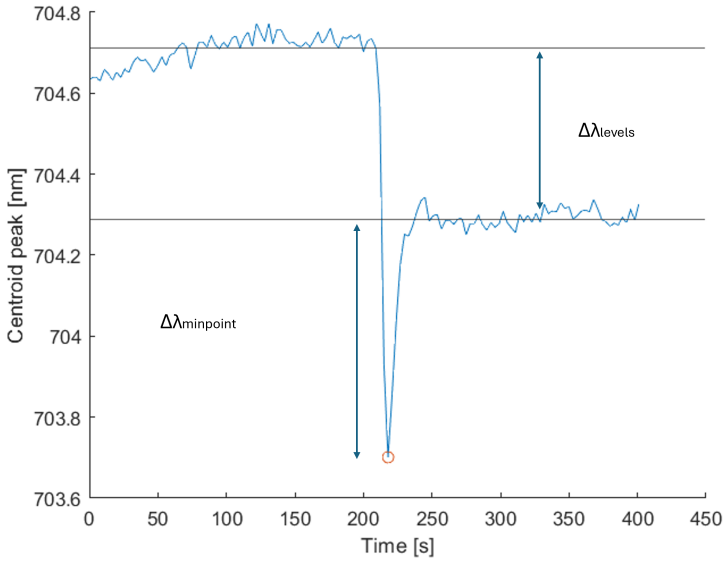

Figure 4.3: Example of how the response to a H_2 pulse looks up-close. The pulse starts at exactly 200 s after which a rapid blueshift of the peak is seen followed by a somewhat smaller redshift. Marked in the graph is the level before the pulse (upper line), the minimal point reached by the blueshift (red circle) and the level after the redshift happens (lower line). The descriptors shown in later figures are calculated from these values. $\Delta\lambda_{minpoint}$ is the difference between the lower level and the minimum point. $\Delta\lambda_{levels}$ is the difference between the two horizontal lines.

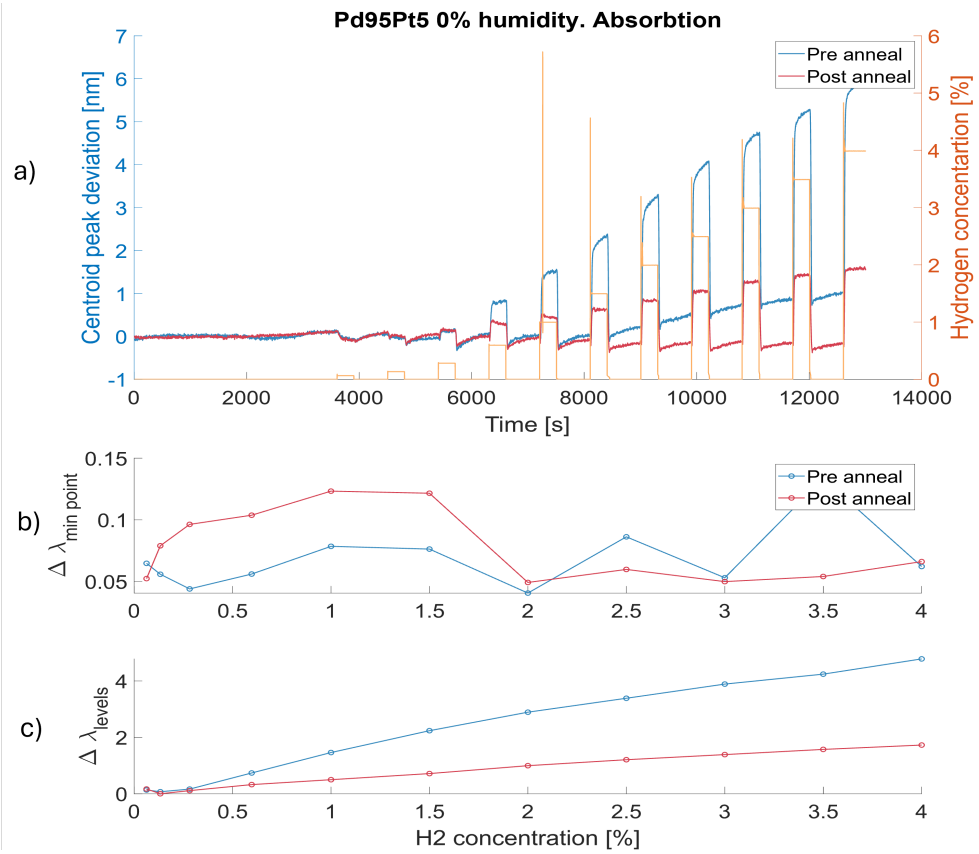

Figure 4.4: Comparison between the annealed and unannealed sample of $Pd_{95}Pt_5$ with 0% humidity. a) hydrogen pulses (orange) and the deviation in centroid peak from base level of the sample, both before annealing (blue) and after (red). b) $\Delta\lambda_{minpoint}$ for the before annealed (blue) and after (red) sample. c) $\Delta\lambda_{levels}$ for the before (blue) and after (red) annealed samples.

Figure 4.4 shows the comparison between the annealed and unannealed $Pd_{95}Pt_5$ samples. The first thing to note in a) is that before annealing, the centroid peak deviation is significantly bigger for each H_2 pulse, and increases faster with increasing H_2 compared to the annealed samples. Another thing to note about the response from the unannealed system is that it keeps monotonically increasing slowly during the entire length of the H_2 pulse, this in contrast to the annealed system that reaches a stable level almost instantly. The reason for this may be that is takes some time to find an equilibrium between the HOR and the adsorbates H and O. However the unannealed system seems to have more of a problem with a drifting baseline as the deviation does not go down to zero between each pulse and keeps increasing, which could be related to the pulse response not reaching an equilibrium. In Figure 4.4 b) $\Delta\lambda_{minpoint}$ can be seen behaving irregularly for both the annealed and unannealed sample. These are however of very small magnitude compared to the $\Delta\lambda_{levels}$ in c), probably only being noise in the signal, and thus have very low impact on the behaviour of the system. These peaks can then be effectively disregarded. In c) we can again see that the unannealed system has a faster increasing optical response to the increasing H_2 pulses than the annealed system. This might be as a result of the annealing Pt atoms being evenly dispersed in the NP. Since the absorbed H

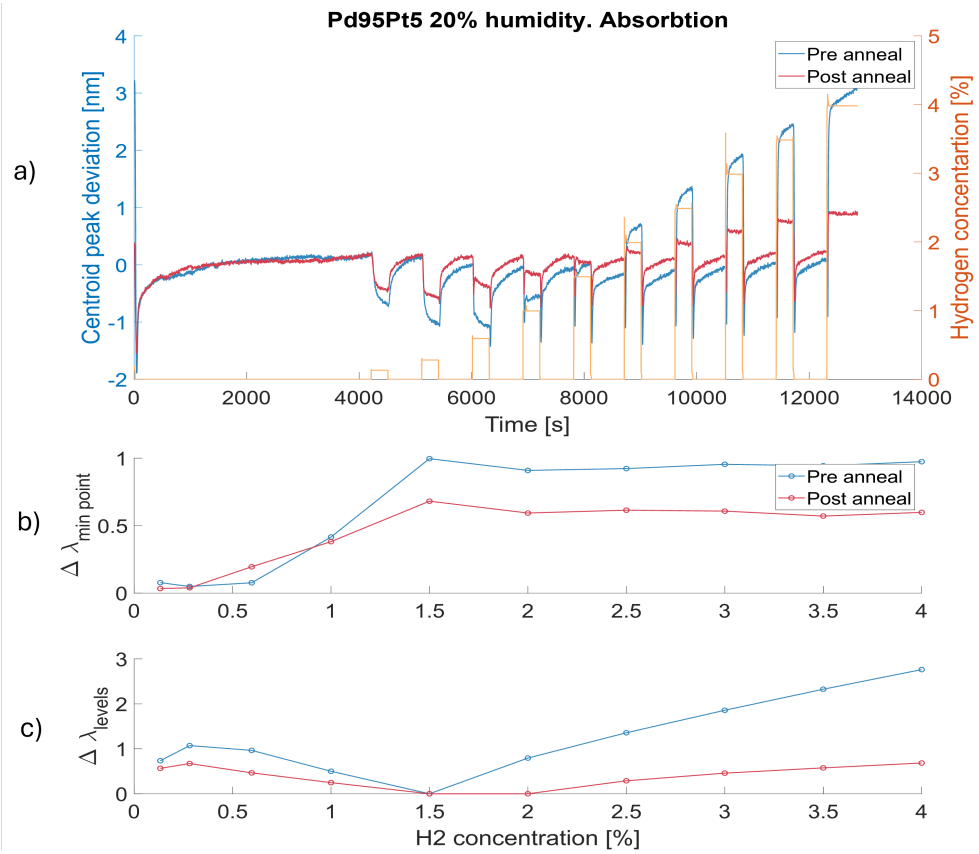

Figure 4.5: Comparison between the annealed and unannealed sample of $Pd_{95}Pt_5$ with 20% humidity. a) hydrogen pulses (orange) and the deviation in centroid peak from base level of the sample, both before annealing (blue) and after (red). b) $\Delta\lambda_{minpoint}$ for the before annealed (blue) and after (red) sample. c) $\Delta\lambda_{levels}$ for the before (blue) and after (red) annealed samples.

wants to form a solid solution around the Pd atoms, having Pt in the mix means less interstitial sites where H "likes" to sit. Both systems do however, seem to scale linearly with the H_2 concentration. According to Sieverts' law the optical response should scale as the square root of the hydrogen pressure [37, 38]. The reason that the relation looks linear may be due to the low H_2 pressures and few data points.

When humidity is introduced into the environment the behaviour of the systems change significantly. The first notable difference seen in Figure 4.5 from the dry conditions is that there now is a clear blueshift for the lower H_2 pulses, which can be seen in a) as well as the now initial peak in $\Delta\lambda_{levels}$ (at the second pulse (0.282 % H_2)) and increasing $\Delta\lambda_{minpoint}$ (now getting a spike as seen in Figure 4.3). This is attributed to the HOR being catalysed by the Pt, reducing the water cover of the NPs. When the H_2 concentration increases however the redshift takes over, this is most likely due to almost all water being removed from the surface of the NPs and hydride formation taking over as the dominant process. Notable is that the hydride formation in the Pd (redshift) seems to take over earlier in the annealed system, clearly showing it is competing against the HOR induced by Pt at the third pulse (0.597 % H_2). In contrast it takes longer for the unannealed system,

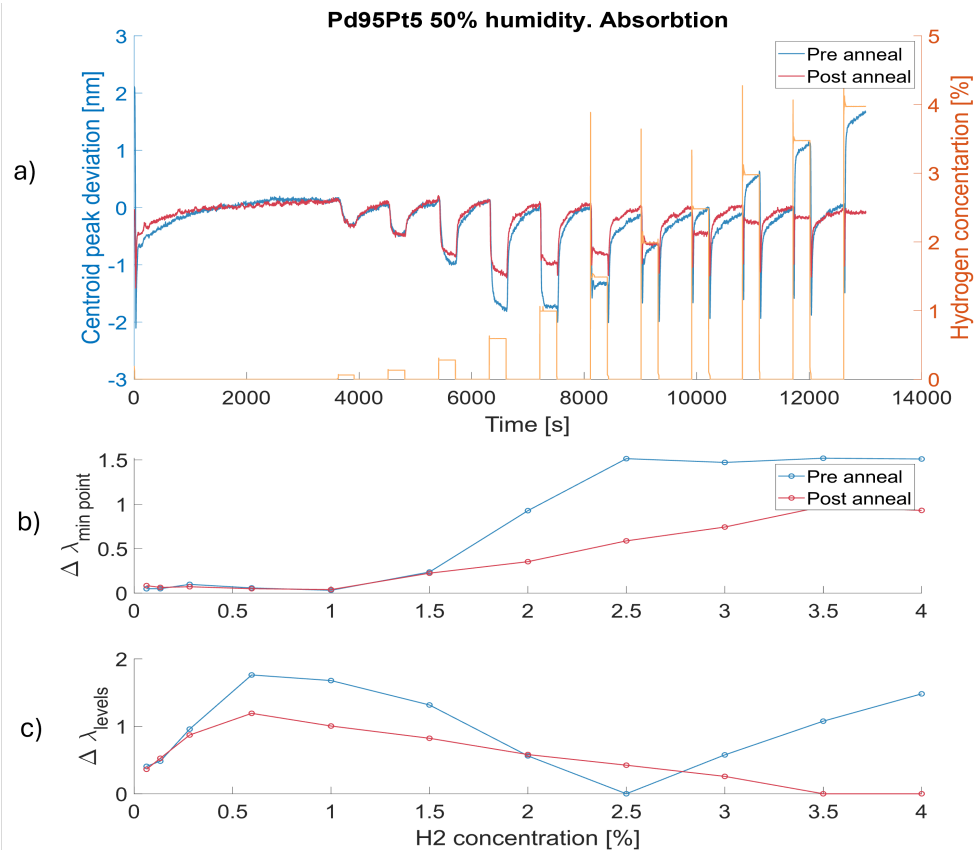

Figure 4.6: Comparison between the annealed and unannealed sample of $Pd_{95}Pt_5$ with 50% humidity. a) hydrogen pulses (orange) and the deviation in centroid peak from base level of the sample, both before annealing (blue) and after (red). b) $\Delta\lambda_{minpoint}$ for the before annealed (blue) and after (red) sample. c) $\Delta\lambda_{levels}$ for the before (blue) and after (red) annealed samples.

not showing clear signs of a hydride formation until the fourth pulse (1 % H_2). This can also be concluded from b) where $\Delta\lambda_{minpoint}$ starts increasing for the annealed sample before it does for the unannealed. After the fifth pulse (1.5 % H_2) both the annealed and unannealed system starts behaving very similar to the dry conditions where $\Delta\lambda_{minpoint}$ holds a stable value and $\Delta\lambda_{levels}$ increases proportional to the H_2 concentration. This is most likely due to that the magnitude of the blueshift caused by the HOR is proportional to both the H_2 concentration and the humidity in the environment, while the redshift due to hydride formation only depends on the H_2 concentration. Meaning that above 1.5 % H_2 there is no longer enough water and O_2 present to keep increasing the response due to the HOR as all the adsorbed (available) H_2 and O_2 likely has been consumed in the HOR already.

One last thing to note in Figure 4.5 is that in the very beginning there is a significant redshift upp to the baseline. This comes from the application of the humidity which gives increases λ_{peak} as discussed in section 2.2.

Further increasing the humidity to 50% shows a continuation of the pattern seen at 20% humidity. In Figure 4.6 a) there is again an initial blueshift due to the HOR occurring on the Pt followed by a redshift at higher H_2 concentrations

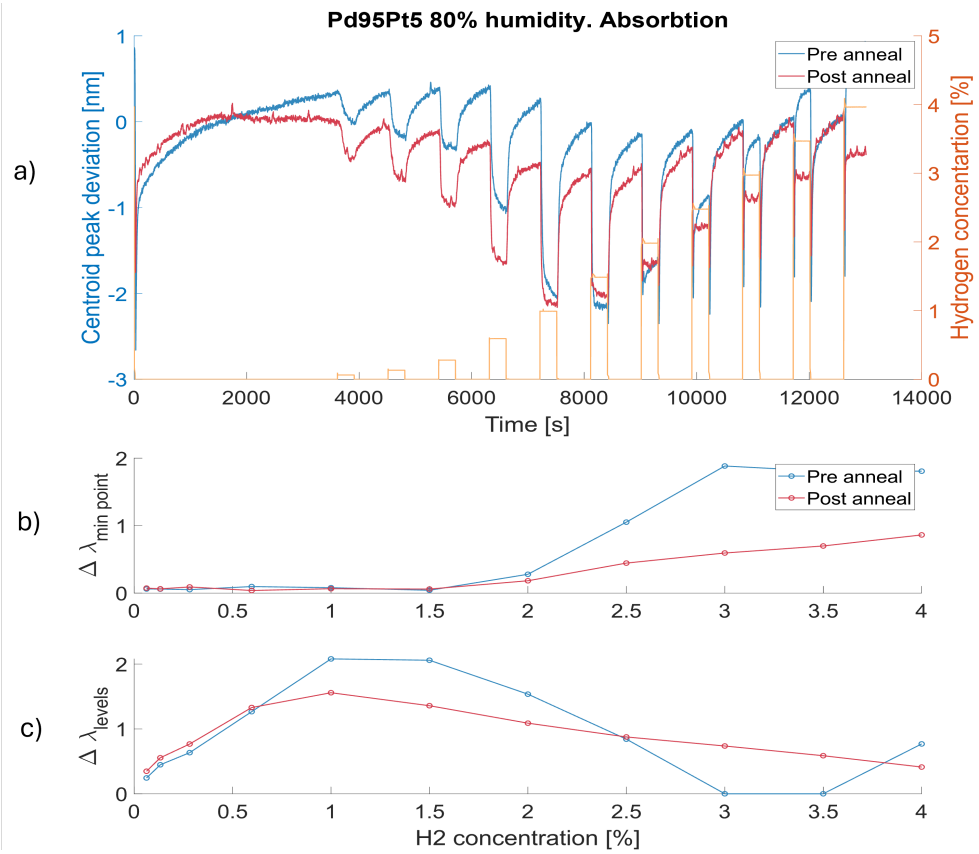

Figure 4.7: Comparison between the annealed and unannealed sample of $Pd_{95}Pt_5$ with 80% humidity. a) hydrogen pulses (orange) and the deviation in centroid peak from base level of the sample, both before annealing (blue) and after (red). b) $\Delta\lambda_{minpoint}$ for the before annealed (blue) and after (red) sample. c) $\Delta\lambda_{levels}$ for the before (blue) and after (red) annealed samples.

due to hydride formation in the Pd. What can be seen is that the point at which hydride formation becomes visible is pushed further into higher concentrations of H_2 compared to at 20 % humidity, now not being clear until the sixth pulse (1.5 % H_2). This is not surprising since with higher humidity more water is expected to be covering the NPs, meaning more hydrogen is needed to remove the H_2O and OH groups before hydride formation can happen. Interestingly the annealed system never reaches a point where the redshift from hydride formation is larger then the blueshift from the HOR at this humidity. While the unannealed system does so at 2.5 % H_2, which can be seen in Figure 4.6 c). This seems to suggest that the unannealed system is more efficient at catalysing the HOR to remove the water and OH to make the H_2 accessible to the Pd for hydride formation.

At 80% humidity, seen in Figure 4.7, the systems again follows the same trends as seen in the lower humidities. Now there are no signs of hydride formation until the seventh pulse (2 % H_2) however. One thing of note in Figure 4.7 that was not present in the earlier graphs (Figure 4.5 and 4.6) is that the baseline drifts down substantially between pulses and seem to still be recovering from the previous pulse when the next one hits. This may be related to the slanted shape, where the optical

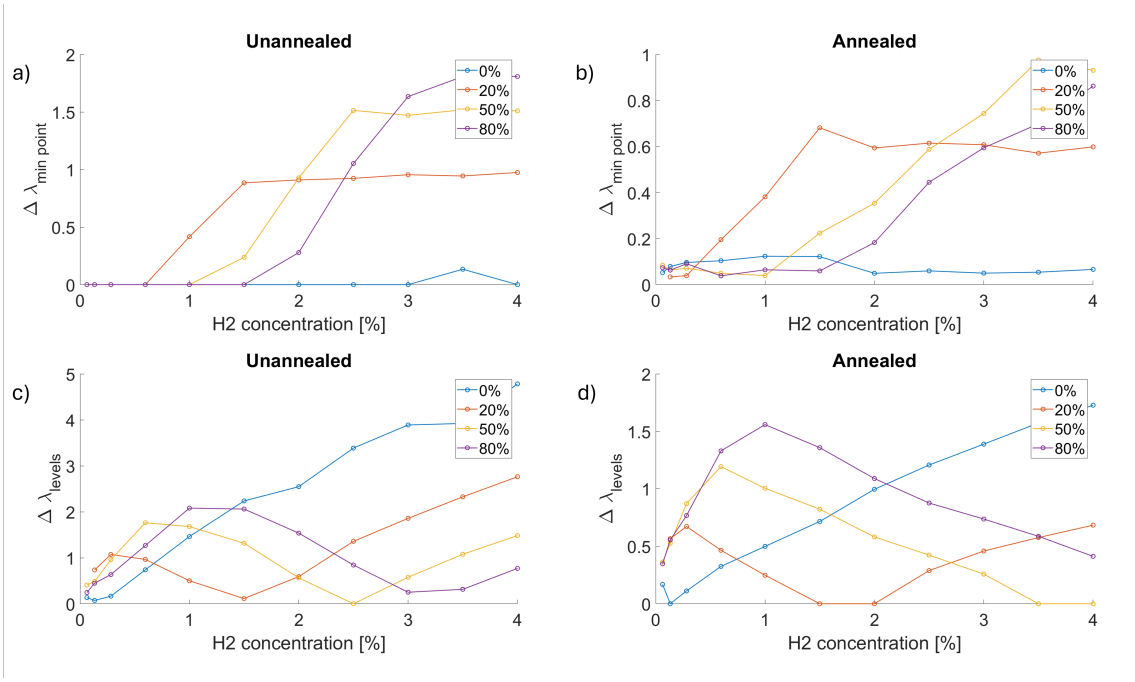

Figure 4.8: Summarising figure showing the descriptors $\Delta\lambda_{minpoint}$ and $\Delta\lambda_{levels}$ for all humidities for both the unannealed and annealed samples. a) and b) shows $\Delta\lambda_{minpoint}$ for all humidities for the unannealed and annealed samples respectively. Here it is clear that for 0% humidity there is no (or close to none) blueshift of the extinction peak. When humidity is present it is clear we get a blueshift that scales to the humidity present. c) and d) shows $\Delta\lambda_{levels}$ for all humidities for the unannealed and annealed samples respectively. Here it is also clear the system behaves very differently in dry conditions compared to in humid conditions. It is also clear that the behaviour in humid conditions scales with level of humidity.

response does not reach a stable level during the H_2 pulse, seen in the response of the unannealed system in the low humidities (0% and 20%) and which the annealed system starts to exhibit from 50% humidity. The reason may be due to the time to reach equilibrium between the HOR removing O, OH and H_2O from the surface and new O_2 and H_2O adsorbing and dissociating again from the background gas. So the competition for the hydrogen being used for HOR and hydride formation may slow down both processes, making it take some time for equilibrium to be reached.

To summarise the different behaviours exhibited by by both the unannealed and annealed samples, the descriptors $\Delta\lambda_{minpoint}$ and $\Delta\lambda_{levels}$ are displayed for all humidities in Figure 4.8. Its clear from a) and b) in Figure 4.8 that for higher humidities it takes longer before both blueshift due to the HOR removing water and redshift from hydride formation occur at the same time, seen in that it takes longer before $\Delta\lambda_{minpoint}$ starts increasing. It is also clear that the lower the humidity the sooner $\Delta\lambda_{minpoint}$ reaches a stable point, corresponding to reaching the most amount o blueshift from HOR possible at that humidity. c) and d) also clearly shows how the humidity level affects when which of the two process (HOR and hydride formation) dominates. Furthermore it is also clear that the unannealed samples give a response with consistently higher magnitude.

5

Conclusion & Outlook

The samples tested ($Pd_{70}Pt_{30}$, $Pd_{85}Pt_{15}$, $Pd_{90}Pt_{10}$ and $Pd_{95}Pt_5$) shows promise as detectors of H_2 in humid environments. Both before and after annealing, the systems are resistant to deactivation by humidity in the surrounding environment, even up to 80 % humidity. With a combination of the descriptors $\Delta\lambda_{minpoint}$ and $\Delta\lambda_{levels}$, one is able to get a linear dependence between the response and the H_2 concentration, which is highly desirable for its ease of interpretation. The difficulty comes from knowing how to best combine these two descriptors, as the switch point is dependent on the humidity level. One way that has been explored in other similar studies would be to utilise a neural network to interpret the data [20].

Furthermore, the unannealed NPs were more catalytically active in the HOR. It is not entirely surprising that the unannealed system is more catalytically active since it has all the Pt at the surface, compared to the annealed system where it would be more evenly spread out in the NP. This means more Pt sites are available for HOR to take place. Though it is not certain if this is a benefit to the detection capabilities of the unannealed system, since neither limits of detection or response time have been investigated here. To investigate this further a more detailed analysis of the difference in response time and limits of detection would be needed. The annealed samples may still be more practical for use as sensors due to them being more likely to be more stable over time. The slightly elevated temperature in the sensor may slowly induce solid state diffusion in the unannealed samples meaning they degrade over time.

Finally, we conclude that Pd-Pt plasmonic nanoparticles, both annealed and non-annealed show great promise as hydrogen sensors in humid conditions. It would however, also be interesting to investigate further how changing the order of the layers (Pt on the bottom instead of the top) in the unannealed samples would affect the HOR and hydride formation.

Bibliography

[1] J. Humphreys, R. Lan, and S. Tao, "Development and recent progress on ammonia synthesis catalysts for haber–bosch process," *Advanced Energy and Sustainability Research*, vol. 2, no. 1, p. 2 000 043, 2021. DOI: https://doi.org/10.1002/aesr.202000043. eprint: https://advanced.onlinelibrary.wiley.com/doi/pdf/10.1002/aesr.202000043. [Online]. Available: https://advanced.onlinelibrary.wiley.com/doi/abs/10.1002/aesr.202000043.

[2] J. O. Bockris, "A hydrogen economy," *Science*, vol. 176, no. 4041, pp. 1323–1323, 1972. DOI: 10.1126/science.176.4041.1323. eprint: https://www.science.org/doi/pdf/10.1126/science.176.4041.1323. [Online]. Available: https://www.science.org/doi/abs/10.1126/science.176.4041.1323.

[3] T. Hübert, L. Boon-Brett, V. Palmisano, and M. A. Bader, "Developments in gas sensor technology for hydrogen safety," *International Journal of Hydrogen Energy*, vol. 39, no. 35, pp. 20 474–20 483, Dec. 2014. DOI: 10.1016/j.ijhydene.2014.05.042.

[4] "Chapter 16 - nanoeffects in ancient technology and art and in space," in *Fundamentals and Applications of Nano Silicon in Plasmonics and Fullerines*, ser. Micro and Nano Technologies, M. Nayfeh, Ed., Elsevier, 2018, pp. 497–518, ISBN: 978-0-323-48057-4. DOI: https://doi.org/10.1016/B978-0-323-48057-4.00016-5. [Online]. Available: https://www.sciencedirect.com/science/article/pii/B9780323480574000165.

[5] G. Mie, "Beiträge zur optik trüber medien, speziell kolloidaler metallösungen," *Annalen der Physik*, vol. 330, no. 3, pp. 377–445, 1908. DOI: https://doi.org/10.1002/andp.19083300302. eprint: https://onlinelibrary.wiley.com/doi/pdf/10.1002/andp.19083300302. [Online]. Available: https://onlinelibrary.wiley.com/doi/abs/10.1002/andp.19083300302.

[6] L. Tong, H. Wei, S. Zhang, and H. Xu, "Recent advances in plasmonic sensors," *Sensors*, vol. 14, no. 5, pp. 7959–7973, 2014, ISSN: 1424-8220. DOI: 10.3390/s140507959. [Online]. Available: https://www.mdpi.com/1424-8220/14/5/7959.

[7] I. Darmadi, F. A. A. Nugroho, and C. Langhammer, "High-performance nanostructured palladium-based hydrogen sensors—current limitations and strategies for their mitigation," *ACS Sensors*, vol. 5, no. 11, pp. 3306–3327, 2020, PMID: 33181012. DOI: 10.1021/acssensors.0c02019. eprint: https://doi.org/10.1021/acssensors.0c02019. [Online]. Available: https://doi.org/10.1021/acssensors.0c02019.

[8] I. Darmadi, "Polymer-nanoparticle hybrid materials for plasmonic hydrogen detection," Ph.D. dissertation, Chalmers universety of thecnology, 2021.

[9] K. M. Mayer and J. H. Hafner, "Localized surface plasmon resonance sensors," *Chemical Reviews*, vol. 111, no. 6, pp. 3828–3857, 2011, PMID: 21648956. DOI: 10.1021/cr100313v. eprint: https://doi.org/10.1021/cr100313v. [Online]. Available: https://doi.org/10.1021/cr100313v.

[10] A. B. Dahlin, J. O. Tegenfeldt, and F. Höök, "Improving the instrumental resolution of sensors based on localized surface plasmon resonance," *Analytical Chemistry*, vol. 78, no. 13, pp. 4416–4423, 2006, PMID: 16808449. DOI: 10.1021/ac0601967. eprint: https://doi.org/10.1021/ac0601967. [Online]. Available: https://doi.org/10.1021/ac0601967.

[11] "Hydrogen factsheet," Center for Sustainable Systems, University of Michigan, Tech. Rep., 2024. [Online]. Available: https://css.umich.edu/publications/factsheets/energy/hydrogen-factsheet.

[12] K. T. Møller, T. R. Jensen, E. Akiba, and H.-w. Li, "Hydrogen - a sustainable energy carrier," *Progress in Natural Science: Materials International*, vol. 27, no. 1, pp. 34–40, 2017, SI-HYDROGEN STORAGE MATERIALS, ISSN: 1002-0071. DOI: https://doi.org/10.1016/j.pnsc.2016.12.014. [Online]. Available: https://www.sciencedirect.com/science/article/pii/S1002007116303240.

[13] U. D. of Energy, "Fuel properties comparison," U.S. Department of Energy, Tech. Rep. [Online]. Available: https://afdc.energy.gov/fuels/properties.

[14] F. D. Manchester, A. San-Martin, and J. M. Pitre, "The h-ta (hydrogen-titanium) system," *Journal of Phase Equilibria*, vol. 8, pp. 30–42, 1987. DOI: 10.1007/BF02868888. [Online]. Available: https://doi.org/10.1007/BF02868888.

[15] F. D. Manchester, A. San-Martin, and J. M. Pitre, "The h-pd (hydrogen-palladium) system," *Journal of Phase Equilibria*, vol. 15, pp. 62–83, 1994. DOI: 10.1007/BF02667685. [Online]. Available: https://doi.org/10.1007/BF02667685.

[16] F. D. Manchester, A. San-Martin, and J. M. Pitre, "The h-ta (hydrogen-tantalum) system," *Journal of Phase Equilibria*, vol. 12, pp. 332–343, 1991. DOI: 10.1007/BF02649922. [Online]. Available: https://doi.org/10.1007/BF02649922.

[17] J. E. Schirber and B. Morosin, "Lattice constants of $\beta - PdH_x$ and $\beta - PdD_x$ with x near 1.0," *Phys. Rev. B*, vol. 12, pp. 117–118, 1 Jul. 1975. DOI: 10.1103/PhysRevB.12.117. [Online]. Available: https://link.aps.org/doi/10.1103/PhysRevB.12.117.

[18] X. Yang, H. Li, R. Ahuja, T. Kang, and W. Luo, "Formation and electronic properties of palladium hydrides and palladium-rhodium dihydride alloys under pressure," *Scientific Reports*, 2017. DOI: 10.1038/s41598-017-02617-z. [Online]. Available: https://www.nature.com/articles/s41598-017-02617-z.

[19] F. D. Manchester, A. San-Martin, and J. M. Pitre, "The h-pd (hydrogen-palladium) system," *Journal of Phase Equilibria*, 1994. DOI: 10.1007/BF02667685. [Online]. Available: https://doi.org/10.1007/BF02667685.

[20] D. Tomecek, H. Moberg, S. Nilsson, and et al., "Neural network enabled nanoplasmonic hydrogen sensors with 100 ppm limit of detection in humid air," *Nature Communications*, vol. 15, 2024. DOI: https://doi.org/10.1038/s41467-024-45484-9. eprint: https://doi.org/10.1038/s41467-024-45484-9. [Online]. Available: https://doi.org/10.1038/s41467-024-45484-9.

[21] C. Wadell, S. Syrenova, and C. Langhammer, "Plasmonic hydrogen sensing with nanostructured metal hydrides," *ACS Nano*, vol. 8, no. 12, pp. 11 925–11 940, 2014, PMID: 25427244. DOI: 10.1021/nn505804f. eprint: https://doi.org/10.1021/nn505804f. [Online]. Available: https://doi.org/10.1021/nn505804f.

[22] E. Hecht, *Optics* (Pearson education). Addison-Wesley, 2002, ISBN: 9780321188786. [Online]. Available: https://books.google.se/books?id=T3ofAQAAMAAJ.

[23] A. Theodoridis, "Nanoplasmonic hydrogen sensors for technologically relevant environments," Ph.D. dissertation, Chalmers universety of thecnology, 2025.

[24] X. Geng *et al.*, "Grain-boundary-rich noble metal nanoparticle assemblies: Synthesis, characterization, and reactivity," *Advanced Functional Materials*, vol. 32, no. 34, p. 2 204 169, 2022. DOI: https://doi.org/10.1002/adfm.202204169. eprint: https://advanced.onlinelibrary.wiley.com/doi/pdf/10.1002/adfm.202204169. [Online]. Available: https://advanced.onlinelibrary.wiley.com/doi/abs/10.1002/adfm.202204169.

[25] G. Korotchenkov, V. Brynzari, and S. Dmitriev, "Electrical behavior of sno2 thin films in humid atmosphere," *Sensors and Actuators B: Chemical*, vol. 54, no. 3, pp. 197–201, 1999, ISSN: 0925-4005. DOI: https://doi.org/10.1016/S0925-4005(99)00016-7. [Online]. Available: https://www.sciencedirect.com/science/article/pii/S0925400599000167.

[26] A. Semerikova *et al.*, "Face-centered cubic platinum hydride and phase diagram of pth," *European Journal of Inorganic Chemistry*, vol. 2020, no. 48, pp. 4532–4538, 2020. DOI: https://doi.org/10.1002/ejic.202000849. eprint: https://chemistry-europe.onlinelibrary.wiley.com/doi/pdf/10.1002/ejic.202000849. [Online]. Available: https://chemistry-europe.onlinelibrary.wiley.com/doi/abs/10.1002/ejic.202000849.

[27] N. M. Marković, T. J. Schmidt, V. Stamenković, and P. N. Ross, "Oxygen reduction reaction on pt and pt bimetallic surfaces: A selective review," *Fuel Cells*, vol. 1, no. 2, pp. 105–116, 2001. DOI: https://doi.org/10.1002/1615-6854(200107)1:2<105::AID-FUCE105>3.0.CO;2-9. eprint: https://onlinelibrary.wiley.com/doi/pdf/10.1002/1615-6854%28200107%291%3A2%3C105%3A%3AAID-FUCE105%3E3.0.CO%3B2-9. [Online]. Available: https://onlinelibrary.wiley.com/doi/abs/10.1002/1615-6854%28200107%291%3A2%3C105%3A%3AAID-FUCE105%3E3.0.CO%3B2-9.

[28] M. Fassihi, V. Zhdanov, M. Rinnemo, K. Keck, and B. Kasemo, "A theoretical and experimental study of catalytic ignition in the hydrogen-oxygen reaction on platinum," *Journal of Catalysis*, vol. 141, no. 2, pp. 438–452, 1993, ISSN: 0021-9517. DOI: https://doi.org/10.1006/jcat.1993.1153. [Online]. Available: https://www.sciencedirect.com/science/article/pii/S002195178371153X.

[29] W. Sheng, H. A. Gasteiger, and Y. Shao-Horn, "Hydrogen oxidation and evolution reaction kinetics on platinum: Acid vs alkaline electrolytes," *Journal of The Electrochemical Society*, vol. 157, no. 11, B1529, Sep. 2010. DOI: 10.1149/1.3483106. [Online]. Available: https://dx.doi.org/10.1149/1.3483106.

[30] Z. Chen *et al.*, "Hydrogen sensors based on pt-decorated sno2 nanorods with fast and sensitive room-temperature sensing performance," *Journal of Alloys and Compounds*, vol. 811, p. 152 086, 2019, ISSN: 0925-8388. DOI: https://doi.org/10.1016/j.jallcom.2019.152086. [Online]. Available: https://www.sciencedirect.com/science/article/pii/S0925838819333328.

[31] A. Harley-Trochimczyk *et al.*, "Catalytic hydrogen sensing using microheated platinum nanoparticle-loaded graphene aerogel," *Sensors and Actuators B: Chemical*, vol. 206, pp. 399–406, 2015, ISSN: 0925-4005. DOI: https://doi.org/10.1016/j.snb.2014.09.057. [Online]. Available: https://www.sciencedirect.com/science/article/pii/S0925400514011265.

[32] B. Hellsing, B. Kasemo, and V. Zhdanov, "Kinetics of the hydrogen-oxygen reaction on platinum," *Journal of Catalysis*, vol. 132, no. 1, pp. 210–228, 1991, ISSN: 0021-9517. DOI: https://doi.org/10.1016/0021-9517(91)90258-6. [Online]. Available: https://www.sciencedirect.com/science/article/pii/0021951791902586.

[33] C. E. Birchenall, "The mechanism of diffusion in the solid state," *Metallurgical Reviews*, vol. 3, no. 1, pp. 235–277, 1958. DOI: 10.1179/mtlr.1958.3.1.235. eprint: https://journals.sagepub.com/doi/pdf/10.1179/mtlr.1958.3.1.235. [Online]. Available: https://journals.sagepub.com/doi/abs/10.1179/mtlr.1958.3.1.235.

[34] Z. Balogh and G. Schmitz, "5 - diffusion in metals and alloys," in *Physical Metallurgy (Fifth Edition)*, D. E. Laughlin and K. Hono, Eds., Fifth Edition, Oxford: Elsevier, 2014, pp. 387–559, ISBN: 978-0-444-53770-6. DOI: https://doi.org/10.1016/B978-0-444-53770-6.00005-8. [Online]. Available: https://www.sciencedirect.com/science/article/pii/B9780444537706000058.

[35] R. F. Mehl, "Rates of diffusion in solid alloys," *Journal of Applied Physics*, vol. 8, no. 3, pp. 174–185, Mar. 1937, ISSN: 0021-8979. DOI: 10.1063/1.1710280. eprint: https://pubs.aip.org/aip/jap/article-pdf/8/3/174/18303445/174_1_online.pdf. [Online]. Available: https://doi.org/10.1063/1.1710280.

[36] H. Fredriksson *et al.*, "Hole–mask colloidal lithography," *Advanced Materials*, vol. 19, no. 23, pp. 4297–4302, 2007. DOI: https://doi.org/10.1002/adma.200700680. eprint: https://advanced.onlinelibrary.wiley.com/doi/pdf/10.1002/adma.200700680. [Online]. Available: https://advanced.onlinelibrary.wiley.com/doi/abs/10.1002/adma.200700680.

[37] I. Zoric´, E. M. Larsson, B. Kasemo, and C. Langhammer, "Localized surface plasmons shed light on nanoscale metal hydrides," *Advanced Materials*, vol. 22, no. 41, pp. 4628–4633, 2010. DOI: https://doi.org/10.1002/adma.201000973. eprint: https://advanced.onlinelibrary.wiley.com/doi/pdf/10.1002/adma.201000973. [Online]. Available: https://advanced.onlinelibrary.wiley.com/doi/abs/10.1002/adma.201000973.

[38] F. A. A. Nugroho, I. Darmadi, V. P. Zhdanov, and C. Langhammer, "Universal scaling and design rules of hydrogen-induced optical properties in pd and pd-alloy nanoparticles," *ACS Nano*, vol. 12, no. 10, pp. 9903–9912, 2018, PMID: 30157370. DOI: 10.1021/acsnano.8b02835. eprint: https://doi.org/10.1021/acsnano.8b02835. [Online]. Available: https://doi.org/10.1021/acsnano.8b02835.

A

Appendix 1

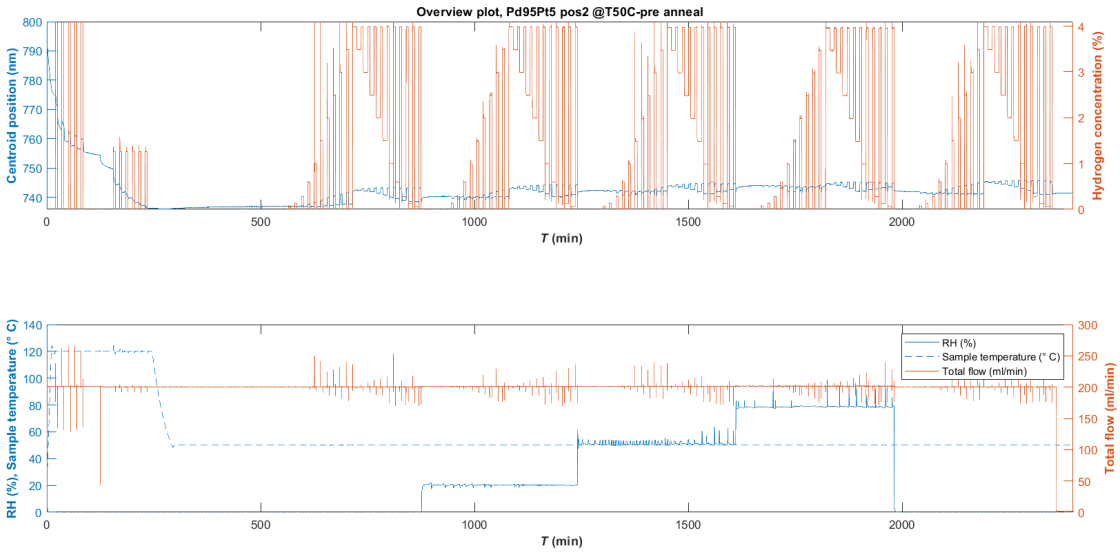

Figure A.1: Overview of the humidity measurments of the $Pd_{95}Pt_5$ sample before annealing.

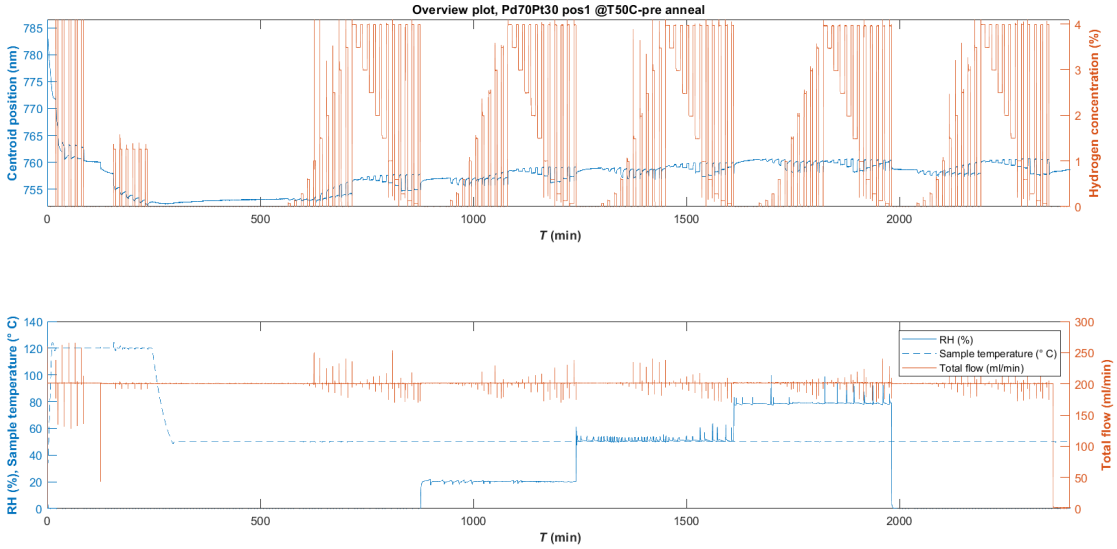

Figure A.2: Overview of the humidity measurments of the $Pd_{70}Pt_{30}$ sample before annealing.

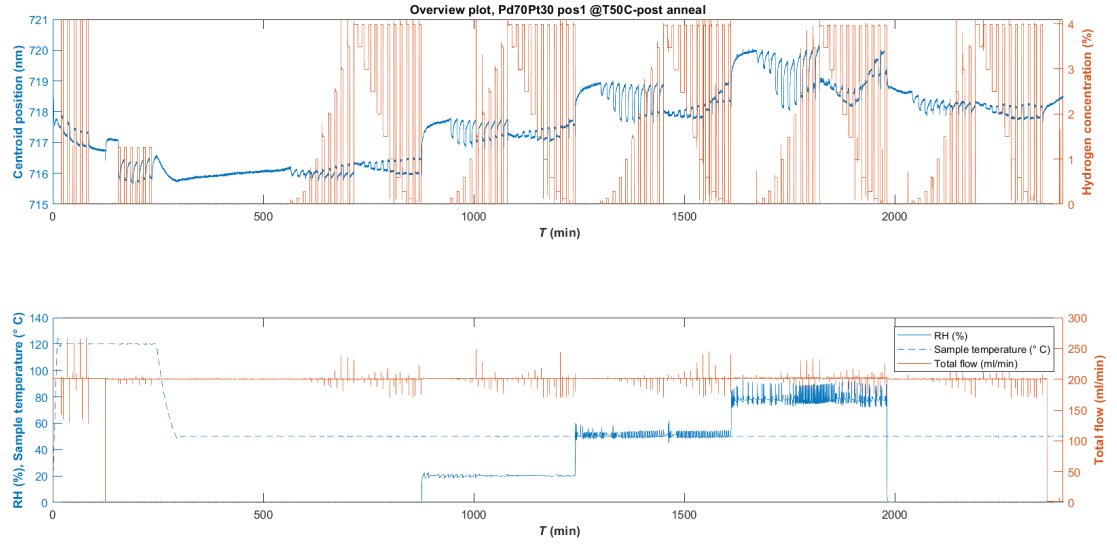

Figure A.3: Overview of the humidity measurments of the $Pd_{70}Pt_{30}$ sample after annealing.

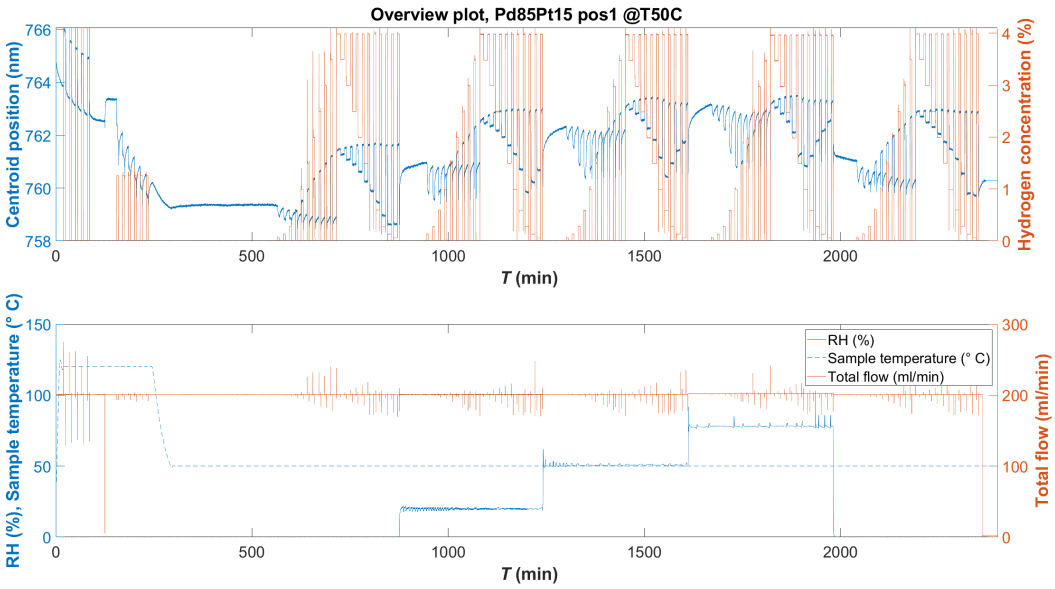

Figure A.4: Overview of the humidity measurments of the $Pd_{85}Pt_{15}$ sample before annealing.

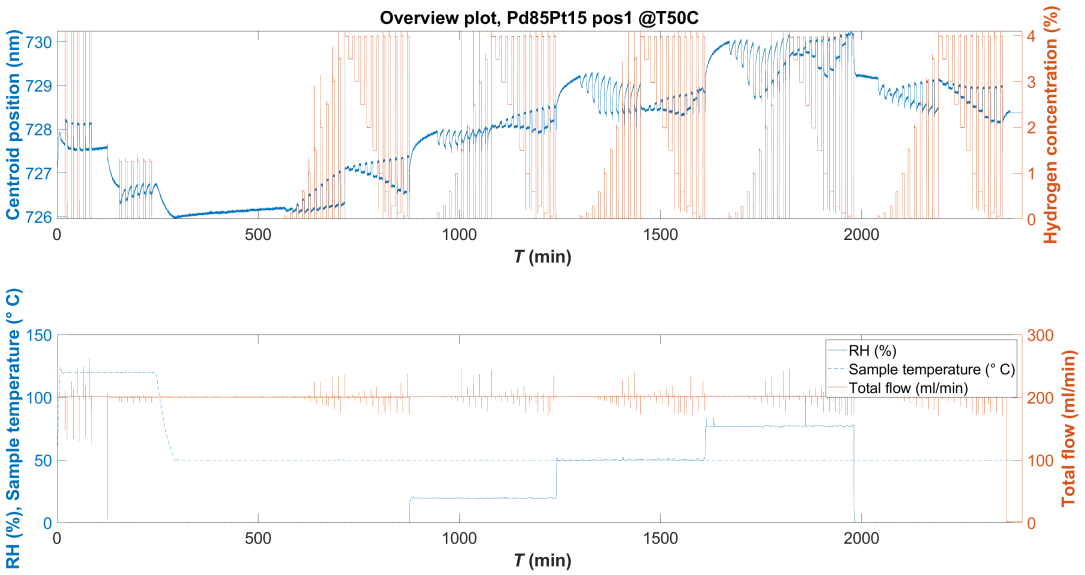

Figure A.5: Overview of the humidity measurments of the $Pd_{85}Pt_{15}$ sample after annealing.

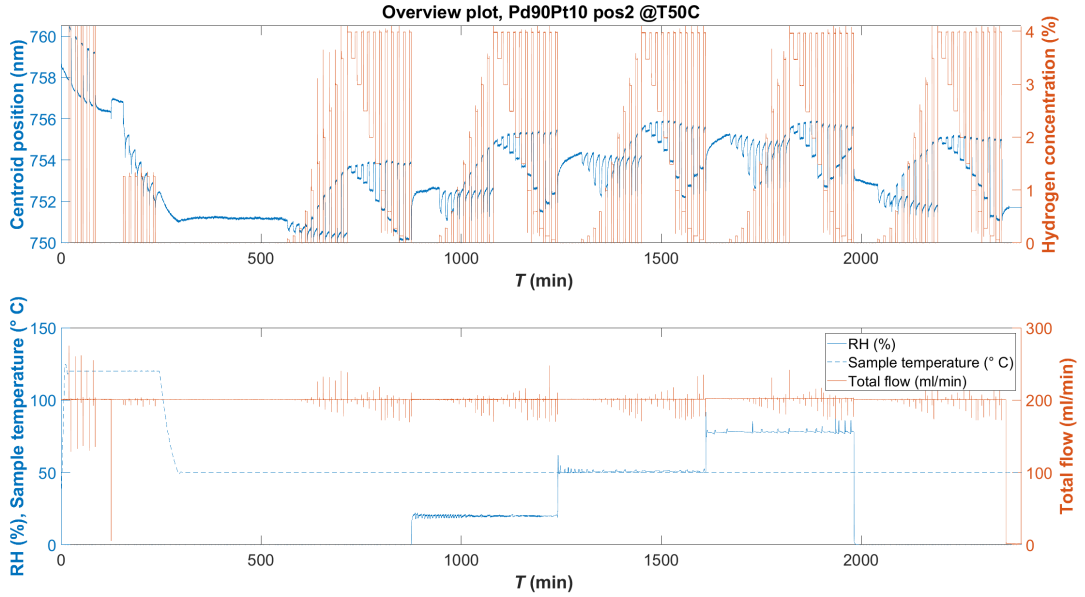

Figure A.6: Overview of the humidity measurments of the $Pd_{90}Pt_{10}$ sample before annealing.

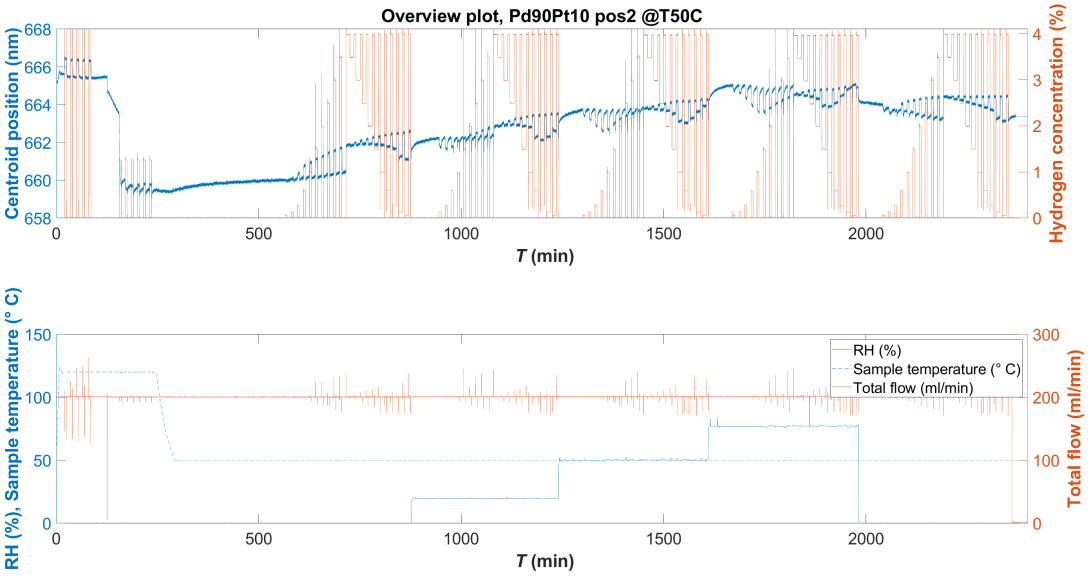

Figure A.7: Overview of the humidity measurments of the $Pd_{90}Pt_{10}$ sample after annealing.

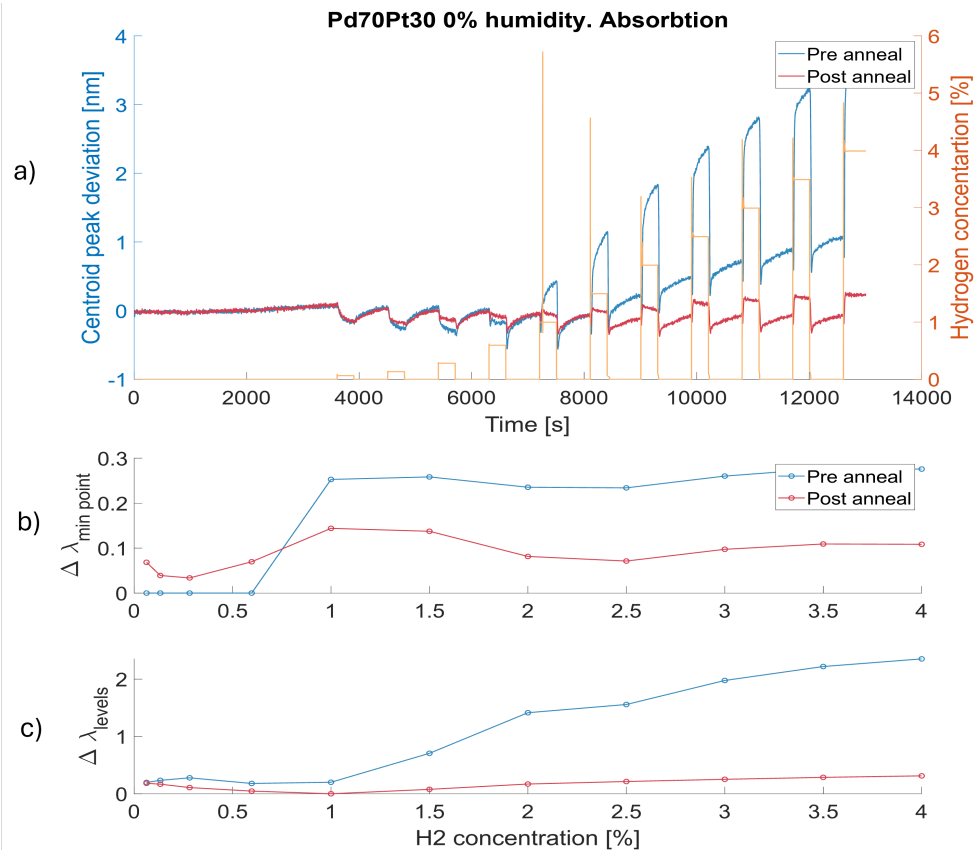

Figure A.8: Comparison between the annealed and unannealed sample of $Pd_{70}Pt_{30}$ with 0% humidity.

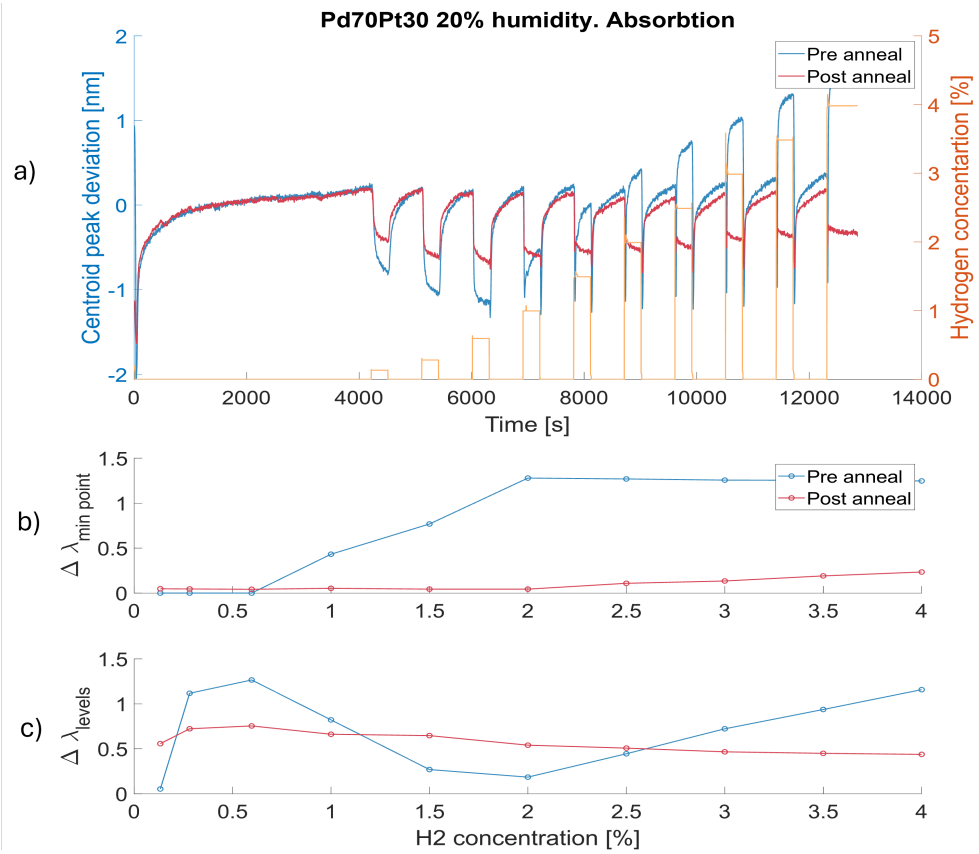

Figure A.9: Comparison between the annealed and unannealed sample of $Pd_{70}Pt_{30}$ with 20% humidity.

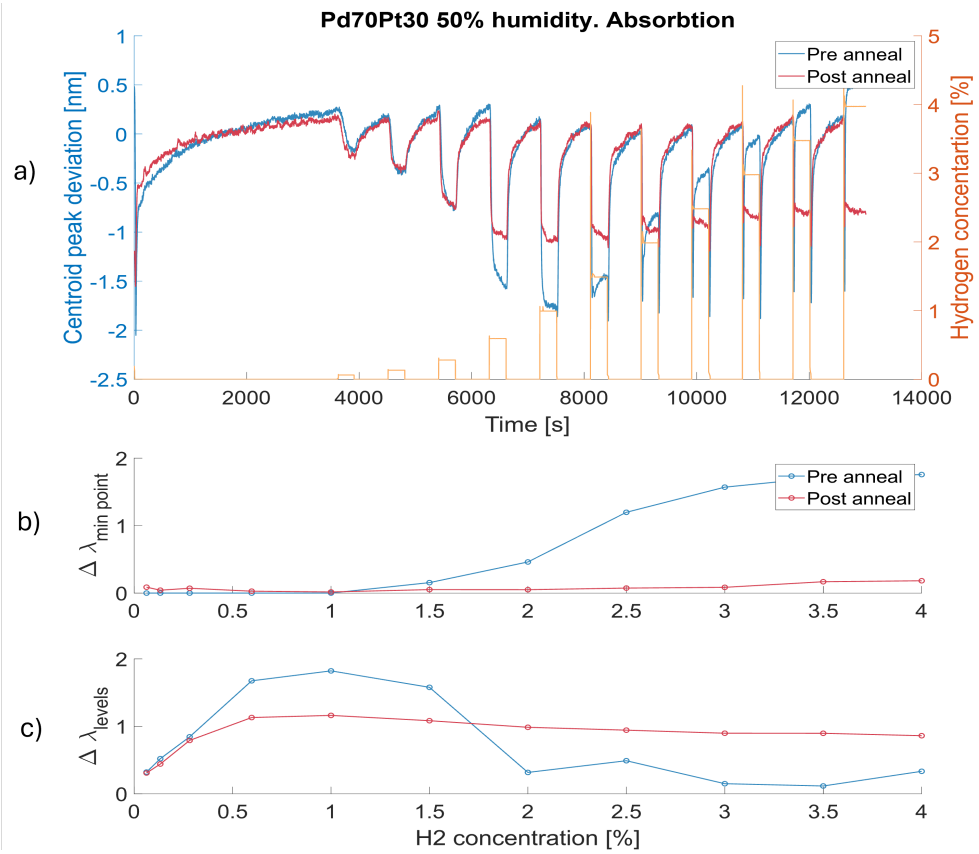

Figure A.10: Comparison between the annealed and unannealed sample of $Pd_{70}Pt_{30}$ with 50% humidity.

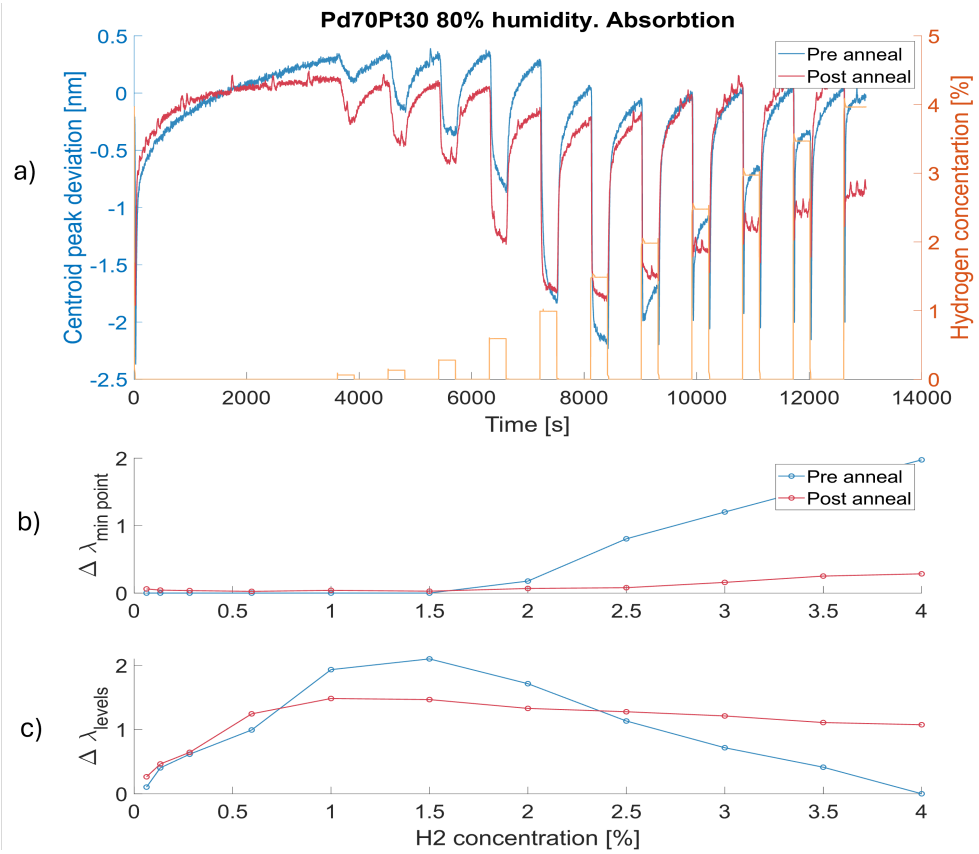

Figure A.11: Comparison between the annealed and unannealed sample of $Pd_{70}Pt_{30}$ with 80% humidity.

DEPARTMENT OF SOME SUBJECT OR TECHNOLOGY
CHALMERS UNIVERSITY OF TECHNOLOGY
Gothenburg, Sweden
www.chalmers.se

CHALMERS
UNIVERSITY OF TECHNOLOGY